

A Regularized Conditional GAN for Posterior Sampling in Inverse Problems

Matthew Bendel
Dept. ECE
The Ohio State University
Columbus, OH 43210
bendel.8@osu.edu

Rizwan Ahmad
Dept. BME
The Ohio State University
Columbus, OH 43210
ahmad.46@osu.edu

Philip Schniter
Dept. ECE
The Ohio State University
Columbus, OH 43210
schniter.1@osu.edu

Abstract

In inverse problems, one seeks to reconstruct an image from incomplete and/or degraded measurements. Such problems arise in magnetic resonance imaging (MRI), computed tomography, deblurring, superresolution, inpainting, and other applications. It is often the case that many image hypotheses are consistent with both the measurements and prior information, and so the goal is not to recover a single “best” hypothesis but rather to explore the space of probable hypotheses, i.e., to sample from the posterior distribution. In this work, we propose a regularized conditional Wasserstein GAN that can generate dozens of high-quality posterior samples per second. Using quantitative evaluation metrics like conditional Fréchet inception distance, we demonstrate that our method produces state-of-the-art posterior samples in both multicoil MRI and inpainting applications.

1. Introduction

This paper considers generative posterior sampling. That is, given a training dataset of input/output pairs $\{(\mathbf{x}_t, \mathbf{y}_t)\}_{t=1}^T$, our goal is to learn a generating function $\hat{\mathbf{x}} = G_\theta(\mathbf{z}, \mathbf{y})$ that, for a given \mathbf{y} , maps random code vectors $\mathbf{z} \sim \mathcal{N}(\mathbf{0}, \mathbf{I})$ to posterior samples $\hat{\mathbf{x}} \sim p_{\mathbf{x}|\mathbf{y}}(\cdot|\mathbf{y})$.

Our interest in posterior sampling is inspired by linear inverse problems, where the goal is to recover a signal or image \mathbf{x} from a measurement \mathbf{y} of the form

$$\mathbf{y} = \mathbf{A}\mathbf{x} + \mathbf{w}, \quad (1)$$

where \mathbf{A} is a known matrix and \mathbf{w} is unknown noise. Such problems arise in deblurring, superresolution, inpainting, computed tomography (CT), magnetic resonance (MR) imaging, and other fields. When \mathbf{A} does not have full column rank, $\mathbf{A}\mathbf{x}$ filters out any components of \mathbf{x} that lie in the nullspace of \mathbf{A} , and so prior information about the true \mathbf{x} is needed for accurate recovery (e.g., we may know that \mathbf{x} is an MR image). But even after taking such prior information

into account, there may be many hypotheses of \mathbf{x} that yield equally good explanations of \mathbf{y} . Thus, rather than settling for a single “best” estimate of \mathbf{x} from \mathbf{y} , our goal is to efficiently sample from the posterior $p_{\mathbf{x}|\mathbf{y}}(\cdot|\mathbf{y})$.

There exist several approaches that learn to sample from the posterior given training samples $\{(\mathbf{x}_t, \mathbf{y}_t)\}_{t=1}^T$, including conditional generative adversarial networks (cGANs) [1, 9, 40, 41], conditional variational autoencoders (cVAEs) [6, 25, 31], conditional normalizing flows (cNFs) [3, 29, 35], and score-based generative models using Langevin dynamics [11, 27, 34]. We focus on cGANs, which are known to generate high-quality samples, but at the expense of sample diversity.

We propose a cGAN that addresses the aforementioned lack-of-diversity issue by training with a novel regularization that enforces consistency with the true posterior mean and covariance. Our proposed regularization consists of supervised ℓ_1 loss plus an appropriately weighted standard-deviation reward. In certain simple cases, the optimal weight can be computed in closed form. For practical settings, we propose a way to automatically calibrate the weight during training.

We demonstrate our approach on accelerated MR image recovery and large-scale image completion/inpainting. To quantify performance, we focus on conditional Fréchet inception distance (CFID) [26], but we also consider FID [8], PSNR, SSIM [33], and average pixel-wise standard deviation (APSD). Our results show the proposed regularized cGAN (rcGAN) outperforming existing cGANs [1, 17, 41] and the state-of-the-art score-based generative models from [11, 27] in all tested metrics.

2. Problem formulation and background

2.1. Conditional Wasserstein GAN

We build on the Wasserstein cGAN framework from [1], noting that the Wasserstein GAN framework [4, 7] has been very successful in avoiding mode collapse and stabilizing the training of GANs. Our goal is to design a generator network $G_\theta : \mathcal{Z} \times \mathcal{Y} \rightarrow \mathcal{X}$ such that, for typical fixed

values of \mathbf{y} , the random variable $\hat{\mathbf{x}} = G_\theta(\mathbf{z}, \mathbf{y})$ induced by $\mathbf{z} \sim p_z$ has a distribution that best matches the posterior $p_{\mathbf{x}|\mathbf{y}}(\cdot|\mathbf{y})$ in the Wasserstein-1 distance. Here, \mathbf{z} is drawn independently of \mathbf{y} , and \mathcal{X} , \mathcal{Y} , and \mathcal{Z} denote the spaces of signals \mathbf{x} , measurements \mathbf{y} , and codes \mathbf{z} , respectively.

The Wasserstein-1 distance can be expressed as [4]

$$W_1(p_{\mathbf{x}|\mathbf{y}}(\cdot, \mathbf{y}), p_{\hat{\mathbf{x}}|\mathbf{y}}(\cdot, \mathbf{y})) = \sup_{D \in L_1} \mathbb{E}_{\mathbf{x}|\mathbf{y}}\{D(\mathbf{x}, \mathbf{y})\} - \mathbb{E}_{\hat{\mathbf{x}}|\mathbf{y}}\{D(\hat{\mathbf{x}}, \mathbf{y})\}, \quad (2)$$

where L_1 denotes functions that are 1-Lipschitz with respect to their first argument and $D : \mathcal{X} \times \mathcal{Y} \rightarrow \mathbb{R}$ is a ‘‘critic’’ or ‘‘discriminator’’ that tries to distinguish between true \mathbf{x} and generated $\hat{\mathbf{x}}$ given \mathbf{y} . Since we seek a method that works for any typical value of \mathbf{y} , we define a loss by taking an expectation of (2) over $\mathbf{y} \sim p_y$. As shown in [1], this expectation commutes with the supremum in (2), so that

$$\mathbb{E}_y\{W_1(p_{\mathbf{x}|\mathbf{y}}(\cdot, \mathbf{y}), p_{\hat{\mathbf{x}}|\mathbf{y}}(\cdot, \mathbf{y}))\} = \sup_{D \in L_1} \mathbb{E}_{\mathbf{x}, \mathbf{y}}\{D(\mathbf{x}, \mathbf{y})\} - \mathbb{E}_{\hat{\mathbf{x}}, \mathbf{y}}\{D(\hat{\mathbf{x}}, \mathbf{y})\} \quad (3)$$

$$= \sup_{D \in L_1} \mathbb{E}_{\mathbf{x}, \mathbf{z}, \mathbf{y}}\{D(\mathbf{x}, \mathbf{y}) - D(G_\theta(\mathbf{z}, \mathbf{y}), \mathbf{y})\}. \quad (4)$$

We then optimize the generator parameters θ to minimize the loss in (4), i.e.,

$$\min_{\theta} \sup_{D \in L_1} \mathbb{E}_{\mathbf{x}, \mathbf{z}, \mathbf{y}}\{D(\mathbf{x}, \mathbf{y}) - D(G_\theta(\mathbf{z}, \mathbf{y}), \mathbf{y})\}. \quad (5)$$

In practice, the discriminator is implemented using a neural network D_ϕ . The parameters θ and ϕ are trained by alternately minimizing

$$\mathcal{L}_{\text{adv}}(\theta, \phi) \triangleq \mathbb{E}_{\mathbf{x}, \mathbf{z}, \mathbf{y}}\{D_\phi(\mathbf{x}, \mathbf{y}) - D_\phi(G_\theta(\mathbf{z}, \mathbf{y}), \mathbf{y})\} \quad (6)$$

with respect to θ and minimizing $-\mathcal{L}_{\text{adv}}(\theta, \phi) + \mathcal{L}_{\text{gp}}(\phi)$ with respect to ϕ , where $\mathcal{L}_{\text{gp}}(\phi)$ is a gradient penalty that is used to encourage $D_\phi \in L_1$ [7]. In practice, the expectation over \mathbf{x} and \mathbf{y} in (6) is replaced by a sample average over the training examples $\{(\mathbf{x}_t, \mathbf{y}_t)\}$.

Mode collapse and regularization. One of the main challenges with the cGAN framework in imaging problems is that, for each training measurement example \mathbf{y}_t there is only a single signal example \mathbf{x}_t . Thus, with the previously described training methodology, there is no incentive for the generator to produce diverse samples $G(\mathbf{z}, \mathbf{y}_t)|_{\mathbf{z} \sim p_z}$ for a given \mathbf{y}_t . This can lead to the generator ignoring the code vector \mathbf{z}_t , which is a form of ‘‘mode collapse.’’

With *unconditional* GANs (uGANs), although mode collapse was historically an issue [16, 21, 23], it was largely solved by the Wasserstein GAN framework [4, 7]. It should be noted that the causes of mode-collapse in uGANs are fundamentally different than in cGANs because, in the uGAN case, the training set $\{\mathbf{x}_t\}$ contains many examples of valid

images, while in the cGAN case there is only *one* example of a valid image \mathbf{x}_t for each given measurement \mathbf{y}_t . As a result, many strategies used to combat mode-collapse in uGANs are not applicable to cGANs. For example, mini-batch discrimination, where the discriminator aims to distinguish a mini-batch of true samples $\{\mathbf{x}_t\}$ from a mini-batch of generated samples $\{\hat{\mathbf{x}}_t\}$ by leveraging inter-sample variation (e.g., MBSD [12] or its precursor from [23]), generally does not work with cGANs because the statistics of the posterior can significantly differ from the statistics of the prior.

To combat mode collapse in the cGAN case, Adler et al. [1] proposed to use a three-input discriminator $D_\phi^{\text{adler}} : \mathcal{X} \times \mathcal{X} \times \mathcal{Y} \rightarrow \mathbb{R}$ and replace \mathcal{L}_{adv} from (6) with the loss

$$\begin{aligned} \mathcal{L}_{\text{adv}}^{\text{adler}}(\theta, \phi) \triangleq & \mathbb{E}_{\mathbf{x}, \mathbf{z}_1, \mathbf{z}_2, \mathbf{y}} \left\{ \frac{1}{2} D_\phi^{\text{adler}}(\mathbf{x}, G_\theta(\mathbf{z}_1, \mathbf{y}), \mathbf{y}) \right. \\ & + \frac{1}{2} D_\phi^{\text{adler}}(G_\theta(\mathbf{z}_2, \mathbf{y}), \mathbf{x}, \mathbf{y}) \\ & \left. - D_\phi^{\text{adler}}(G_\theta(\mathbf{z}_1, \mathbf{y}), G_\theta(\mathbf{z}_2, \mathbf{y}), \mathbf{y}) \right\}, \quad (7) \end{aligned}$$

which rewards variation between the first and second inputs of D_ϕ^{adler} . They then proved that minimizing $\mathcal{L}_{\text{adv}}^{\text{adler}}$ in place of \mathcal{L}_{adv} does not compromise the Wasserstein cGAN objective, i.e., $\arg \min_{\theta} \mathcal{L}_{\text{adv}}^{\text{adler}}(\theta, \phi) = \arg \min_{\theta} \mathcal{L}_{\text{adv}}(\theta, \phi)$.

Ohayon et al. [17] proposed to fight mode collapse via supervised- ℓ_2 regularization¹ of \mathcal{L}_{adv} , i.e., by solving $\arg \min_{\theta} \{\mathcal{L}_{\text{adv}}(\theta, \phi) + \lambda \mathcal{L}_2(\theta)\}$ with some $\lambda > 0$ and

$$\mathcal{L}_2(\theta) \triangleq \mathbb{E}_{\mathbf{x}, \mathbf{y}} \left\{ \|\mathbf{x} - \mathbb{E}_{\mathbf{z}}\{G_\theta(\mathbf{z}, \mathbf{y})\}\|_2^2 \right\} \quad (8)$$

when training the generator. As explained in [17], this regularization is consistent with the cGAN objective in that: if there exists some θ for which $p_{\hat{\mathbf{x}}|\mathbf{y}}$ matches the true posterior $p_{\mathbf{x}|\mathbf{y}}$ (recall that $\hat{\mathbf{x}} \triangleq G_\theta(\mathbf{z}, \mathbf{y})|_{\mathbf{z} \sim p_z}$) then both \mathcal{L}_{adv} and \mathcal{L}_2 are minimized by the same θ . This is because $\mathcal{L}_2(\theta)$ is minimized when $\mathbb{E}_{\mathbf{z}}\{G_\theta(\mathbf{z}, \mathbf{y})\}$ is the minimum mean-square error (MMSE) estimate of \mathbf{x} from \mathbf{y} , or equivalently the posterior mean $\mathbb{E}_{\mathbf{x}|\mathbf{y}}\{\mathbf{x}|\mathbf{y}\}$. So, both \mathcal{L}_{adv} and \mathcal{L}_2 are minimized by the θ for which G_θ samples from the true posterior $p_{\mathbf{x}|\mathbf{y}}$, if such a θ exists. In practice, such a θ may not exist, in which case \mathcal{L}_{adv} and \mathcal{L}_2 will act in complementary ways to drive G_θ towards the true-posterior generator.

It is important to note that practical application requires the use of a (finite) P -sample average with $P \geq 2$ (e.g., $P = 8$ in Ohayon [18]), i.e.,

$$\mathcal{L}_{2, P}(\theta) \triangleq \mathbb{E}_{\mathbf{x}, \mathbf{z}_1, \dots, \mathbf{z}_P, \mathbf{y}} \left\{ \left\| \mathbf{x} - \frac{1}{P} \sum_{i=1}^P G_\theta(\mathbf{z}_i, \mathbf{y}) \right\|_2^2 \right\}. \quad (9)$$

in place of the expectation $\mathbb{E}_{\mathbf{z}}$ in (8). As we show below, $\mathcal{L}_{2, P}$ has the potential to *induce* mode collapse rather than prevent it, and the potential grows larger as P grows smaller.

The problem with supervised- ℓ_2 regularization. To understand why supervised- ℓ_2 regularization using a finite-sample average can lead to mode collapse, we rewrite (9)

¹The idea to regularize a cGAN with supervised- ℓ_2 loss was proposed long before [17]; see, e.g., [9].

as

$$\begin{aligned}\mathcal{L}_{2,P}(\boldsymbol{\theta}) &= \mathbb{E}_{\mathbf{y}} \left\{ \mathbb{E}_{\mathbf{x}, \mathbf{z}_1, \dots, \mathbf{z}_P | \mathbf{y}} \left\{ \|\mathbf{x} - \widehat{\mathbf{x}}_{(P)}\|_2^2 | \mathbf{y} \right\} \right\} \quad (10) \\ &= \mathbb{E}_{\mathbf{y}} \left\{ \|\widehat{\mathbf{x}}_{\text{mmse}} - \bar{\mathbf{x}}\|_2^2 + \frac{1}{P} \mathbb{E}_{\mathbf{z}_i | \mathbf{y}} \left\{ \|\mathbf{d}_i\|_2^2 | \mathbf{y} \right\} \right. \\ &\quad \left. + \mathbb{E}_{\mathbf{x} | \mathbf{y}} \left\{ \|\mathbf{e}_{\text{mmse}}\|_2^2 | \mathbf{y} \right\} \right\} \quad (11)\end{aligned}$$

(see Appendix A for a derivation) using

$$\begin{aligned}\widehat{\mathbf{x}}_i &\triangleq G_{\boldsymbol{\theta}}(\mathbf{z}_i, \mathbf{y}), & \widehat{\mathbf{x}}_{(P)} &\triangleq \frac{1}{P} \sum_{i=1}^P \widehat{\mathbf{x}}_i, \\ \bar{\mathbf{x}} &\triangleq \mathbb{E}_{\mathbf{z}_i | \mathbf{y}} \{\widehat{\mathbf{x}}_i | \mathbf{y}\}, & \bar{\mathbf{x}} &= \mathbb{E}_{\mathbf{z}_1, \dots, \mathbf{z}_P | \mathbf{y}} \{\widehat{\mathbf{x}}_{(P)} | \mathbf{y}\}, \\ \mathbf{d}_i &\triangleq \widehat{\mathbf{x}}_i - \bar{\mathbf{x}}, & \mathbf{d}_{(P)} &\triangleq \frac{1}{P} \sum_{i=1}^P \mathbf{d}_i, \\ \widehat{\mathbf{x}}_{\text{mmse}} &\triangleq \mathbb{E}_{\mathbf{x} | \mathbf{y}} \{\mathbf{x} | \mathbf{y}\}, & \mathbf{e}_{\text{mmse}} &\triangleq \mathbf{x} - \widehat{\mathbf{x}}_{\text{mmse}},\end{aligned} \quad (12)$$

noting that $\mathbb{E}_{\mathbf{z}_i | \mathbf{y}} \{\widehat{\mathbf{x}}_i | \mathbf{y}\}$ is invariant to i since $\{\mathbf{z}_i\}$ are i.i.d.

Let us now examine (11). First, note that only $\bar{\mathbf{x}}$ and \mathbf{d}_i in (11) depend on the generator parameters $\boldsymbol{\theta}$. The first term in (11) encourages $\bar{\mathbf{x}}$ to match the MMSE estimate $\widehat{\mathbf{x}}_{\text{mmse}}$, while the second term in (11) encourages $\mathbf{d}_i = \mathbf{0}$ or equivalently $\widehat{\mathbf{x}}_i = \bar{\mathbf{x}}$, which corresponds to mode collapse. Important observations are

1. As P decreases, $\mathcal{L}_{2,P}$ gives a stronger incentive to mode collapse (due to the $1/P$ term in (11)).
2. In the limit of $P \rightarrow \infty$, $\mathcal{L}_{2,P}$ gives no incentive to mode collapse, but also no disincentive.

Experimentally, we observe that supervised- ℓ_2 regularization does indeed lead to mode collapse when $P = 2$. Although mode collapse may not occur with larger values of P , there is a high computational cost to using large P as a result of GPU memory constraints: as P doubles, the batch size must halve, and so training time increases linearly with P . For example, in our MRI experiment, we found that $P = 2$ takes approximately 2.5 days to train for 100 epochs on a $4 \times \text{A100}$ GPU server, while $P = 8$ takes approximately 10 days.

Does a variance reward help? To mitigate $\mathcal{L}_{2,P}$'s incentive for mode-collapse, one might try to incorporate a variance reward. In particular, to train the generator, one could solve

$$\arg \min_{\boldsymbol{\theta}} \left\{ \beta_{\text{adv}} \mathcal{L}_{\text{adv}}(\boldsymbol{\theta}, \phi) + \mathcal{L}_{2,\text{var},P}(\boldsymbol{\theta}, \beta_{\text{var}}) \right\} \quad (13)$$

with some $\beta_{\text{adv}}, \beta_{\text{var}} > 0$ and $P \geq 2$ using

$$\mathcal{L}_{2,\text{var},P}(\boldsymbol{\theta}, \beta_{\text{var}}) \triangleq \mathcal{L}_{2,P}(\boldsymbol{\theta}) - \beta_{\text{var}} \mathcal{L}_{\text{var},P}(\boldsymbol{\theta}) \quad (14)$$

$$\mathcal{L}_{\text{var},P}(\boldsymbol{\theta}) \triangleq \frac{1}{P-1} \sum_{i=1}^P \mathbb{E}_{\mathbf{z}_1, \dots, \mathbf{z}_P, \mathbf{y}} \left\{ \|\widehat{\mathbf{x}}_i - \widehat{\mathbf{x}}_{(P)}\|_2^2 \right\}. \quad (15)$$

We show in Appendix B that (15) can be rewritten as

$$\mathcal{L}_{\text{var},P}(\boldsymbol{\theta}) = \mathbb{E}_{\mathbf{y}} \left\{ \mathbb{E}_{\mathbf{z}_i | \mathbf{y}} \left\{ \|\mathbf{d}_i\|_2^2 | \mathbf{y} \right\} \right\}, \quad (16)$$

with \mathbf{d}_i from (12), so that

$$\begin{aligned}\mathcal{L}_{2,\text{var},P}(\boldsymbol{\theta}, \beta_{\text{var}}) &= \mathbb{E}_{\mathbf{y}} \left\{ \|\widehat{\mathbf{x}}_{\text{mmse}} - \bar{\mathbf{x}}\|_2^2 \right. \\ &\quad \left. + \left(\frac{1}{P} - \beta_{\text{var}} \right) \mathbb{E}_{\mathbf{z}_i | \mathbf{y}} \left\{ \|\mathbf{d}_i\|_2^2 | \mathbf{y} \right\} + \mathbb{E}_{\mathbf{x} | \mathbf{y}} \left\{ \|\mathbf{e}_{\text{mmse}}\|_2^2 | \mathbf{y} \right\} \right\}.\end{aligned} \quad (17)$$

From (17), we can see that minimizing the regularization $\mathcal{L}_{2,\text{var},P}(\boldsymbol{\theta}, \beta_{\text{var}})$ with $\beta_{\text{var}} = 1/P$ encourages $\bar{\mathbf{x}}$ to match the MMSE estimate $\widehat{\mathbf{x}}_{\text{mmse}}$ without encouraging or discouraging mode collapse. To discourage mode collapse, one might consider using $\beta_{\text{var}} > 1/P$, but in this case $\mathcal{L}_{2,\text{var},P}(\boldsymbol{\theta}, \beta_{\text{var}})$ would encourage the norm of \mathbf{d}_i (i.e., trace covariance of $\widehat{\mathbf{x}}_i$) to be as large as possible, which is not our aim. We want a regularizer that encourages the covariance of $\widehat{\mathbf{x}}_i$ to match the true posterior covariance, but it is not clear that this can be accomplished using $\mathcal{L}_{2,P}$ -based regularization.

2.2. Quantifying performance using CFID

As previously stated, our goal is to train a generator $G_{\boldsymbol{\theta}}$ so that, for typical fixed values of \mathbf{y} , the distribution $p_{\widehat{\mathbf{x}} | \mathbf{y}}$ matches the true posterior $p_{\mathbf{x} | \mathbf{y}}(\cdot | \mathbf{y})$. It is essential to have a quantitative metric for evaluating performance with respect to this goal. For example, it is not enough that the generated samples are ‘‘accurate’’ in the sense that $\widehat{\mathbf{x}}_i$ or $\widehat{\mathbf{x}}_{(P)}$ are close to the ground truth \mathbf{x} , nor is it enough that $\widehat{\mathbf{x}}_i$ are ‘‘diverse’’ in the sense of having a large element-wise standard deviation.

Thus, we quantify the performance of posterior approximation using the conditional Fréchet inception distance (CFID) [26], which is a computationally efficient approximation to the conditional Wasserstein distance (CWD)

$$\text{CWD} \triangleq \mathbb{E}_{\mathbf{y}} \left\{ W_2(p_{\mathbf{x} | \mathbf{y}}(\cdot, \mathbf{y}), p_{\widehat{\mathbf{x}} | \mathbf{y}}(\cdot, \mathbf{y})) \right\}. \quad (18)$$

In (18), $W_2(p_a, p_b)$ denotes the Wasserstein-2 distance between distributions p_a and p_b , defined as

$$W_2(p_a, p_b) \triangleq \min_{p_{a,b} \in \Pi(p_a, p_b)} \mathbb{E}_{\mathbf{a}, \mathbf{b}} \left\{ \|\mathbf{a} - \mathbf{b}\|_2^2 \right\} \quad (19)$$

$$\Pi(p_a, p_b) \triangleq \left\{ p_{a,b} : p_a = \int p_{a,b} d\mathbf{b} \text{ and } p_b = \int p_{a,b} d\mathbf{a} \right\},$$

where $\Pi(p_a, p_b)$ denotes the set of joint distributions $p_{a,b}$ with prescribed marginals p_a and p_b . Similar to how the Fréchet inception distance (FID) [8]—a popular method used to evaluate unconditional GAN performance—is computed, CFID approximates CWD (18) as follows: i) the random vectors \mathbf{x} and $\widehat{\mathbf{x}}$ are replaced by low-dimensional embeddings $\underline{\mathbf{x}}$ and $\underline{\widehat{\mathbf{x}}}$, typically generated using the Inception v3 network [30], and ii) the embedding distributions $p_{\underline{\mathbf{x}} | \mathbf{y}}$ and $p_{\underline{\widehat{\mathbf{x}}} | \mathbf{y}}$ are approximated by Gaussians $\mathcal{N}(\boldsymbol{\mu}_{\underline{\mathbf{x}} | \mathbf{y}}, \boldsymbol{\Sigma}_{\underline{\mathbf{x}} | \mathbf{y}})$ and $\mathcal{N}(\boldsymbol{\mu}_{\underline{\widehat{\mathbf{x}}} | \mathbf{y}}, \boldsymbol{\Sigma}_{\underline{\widehat{\mathbf{x}}} | \mathbf{y}})$. With these approximations, the CWD reduces to

$$\begin{aligned}\text{CFID} &\triangleq \mathbb{E}_{\mathbf{y}} \left\{ \|\boldsymbol{\mu}_{\underline{\mathbf{x}} | \mathbf{y}} - \boldsymbol{\mu}_{\underline{\widehat{\mathbf{x}}} | \mathbf{y}}\|_2^2 + \text{tr} \left[\boldsymbol{\Sigma}_{\underline{\mathbf{x}} | \mathbf{y}} + \boldsymbol{\Sigma}_{\underline{\widehat{\mathbf{x}}} | \mathbf{y}} \right. \right. \\ &\quad \left. \left. - 2 \left(\boldsymbol{\Sigma}_{\underline{\mathbf{x}} | \mathbf{y}}^{1/2} \boldsymbol{\Sigma}_{\underline{\widehat{\mathbf{x}}} | \mathbf{y}} \boldsymbol{\Sigma}_{\underline{\mathbf{x}} | \mathbf{y}}^{1/2} \right)^{1/2} \right] \right\}.\end{aligned} \quad (20)$$

In practice, the expectations, means, and covariances in (20) are replaced by sample averages using samples $\{(\mathbf{x}_t, \mathbf{y}_t)\}$ from a test set. For more on CFID, please see Appendix E.

3. Proposed method

3.1. Regularization: Supervised- ℓ_1 plus standard-deviation reward

We now propose a different form of cGAN regularization that, unlike those previously discussed, encourages the samples $\hat{\mathbf{x}}_i$ to match the true posterior in both mean and covariance. In particular, when training the generator, we propose to solve

$$\arg \min_{\theta} \{ \beta_{\text{adv}} \mathcal{L}_{\text{adv}}(\theta, \phi) + \mathcal{L}_{1,\text{std},P}(\theta, \beta_{\text{std}}) \} \quad (21)$$

with some $\beta_{\text{adv}}, \beta_{\text{std}} > 0$ and $P \geq 2$, where regularizer

$$\mathcal{L}_{1,\text{std},P}(\theta, \beta_{\text{std}}) \triangleq \mathcal{L}_{1,P}(\theta) - \beta_{\text{std}} \mathcal{L}_{\text{std},P}(\theta) \quad (22)$$

is constructed from P -sample supervised- ℓ_1 loss and standard-deviation reward:

$$\mathcal{L}_{1,P}(\theta) \triangleq \mathbb{E}_{\mathbf{x}, z_1, \dots, z_P, \mathbf{y}} \{ \|\mathbf{x} - \hat{\mathbf{x}}_{(P)}\|_1 \} \quad (23)$$

$$\mathcal{L}_{\text{std},P}(\theta) \triangleq \sqrt{\frac{\pi}{2P(P-1)}} \sum_{i=1}^P \mathbb{E}_{z_1, \dots, z_P, \mathbf{y}} \{ \|\hat{\mathbf{x}}_i - \hat{\mathbf{x}}_{(P)}\|_1 \}, \quad (24)$$

where $\hat{\mathbf{x}}_i$ and $\hat{\mathbf{x}}_{(P)}$ were defined in (12).

In practice, we find that $P = 2$ works best (in accordance with Fig. 1). From a computational perspective, this is highly advantageous because, as discussed earlier, the time to train the network increases linearly with P .

We note that regularizing a cGAN with supervised- ℓ_1 loss alone is not new; see, e.g., [9, 40]. In fact, for image recovery in general, the use of supervised- ℓ_1 loss is often preferred over ℓ_2 because it results in sharper, more visually pleasing results [39]. But regularizing a cGAN using supervised- ℓ_1 loss alone can push the generator towards mode collapse, for reasons similar to the supervised- ℓ_2 case discussed earlier. For example, ℓ_1 -induced mode collapse was observed in [9], which led the authors to use dropout instead of random codes z_i to induce variation in the generator output.

Our contribution is to use a properly weighted standard-deviation (std) reward in conjunction with supervised- ℓ_1 loss, as in (22). As we show below, under certain assumptions, the std reward works together with the ℓ_1 loss to enforce the correctness of both the posterior mean *and* the posterior covariance. This stands in contrast to the case of ℓ_2 loss with a variance reward, which enforces only the correctness of the posterior mean.

Proposition 1. Assume that $P \geq 2$ and that θ has complete control over the \mathbf{y} -conditional mean and covariance of $\hat{\mathbf{x}}_i$. Then the regularization-minimizing parameters $\theta_* = \arg \min_{\theta} \mathcal{L}_{1,\text{std},P}(\theta, \beta_{\text{std}}^N)$ with

$$\beta_{\text{std}}^N \triangleq \sqrt{\frac{2}{\pi P(P+1)}} \quad (25)$$

yield generated statistics

$$\mathbb{E}_{z_i | \mathbf{y}} \{ \hat{\mathbf{x}}_i(\theta_*) | \mathbf{y} \} = \mathbb{E}_{\mathbf{x} | \mathbf{y}} \{ \mathbf{x} | \mathbf{y} \} = \hat{\mathbf{x}}_{\text{mmse}} \quad (26a)$$

$$\text{Cov}_{z_i | \mathbf{y}} \{ \hat{\mathbf{x}}_i(\theta_*) | \mathbf{y} \} = \text{Cov}_{\mathbf{x} | \mathbf{y}} \{ \mathbf{x} | \mathbf{y} \} \quad (26b)$$

when the elements of $\hat{\mathbf{x}}_i$ and \mathbf{x} are independent Gaussian conditioned on \mathbf{y} . Thus, the $\mathcal{L}_{1,\text{std},P}$ regularization encourages the \mathbf{y} -conditional mean and covariance of $\hat{\mathbf{x}}_i$ to match those of the true \mathbf{x} .

Proof. See Appendix C. \square

In most applications, $\hat{\mathbf{x}}_i$ and \mathbf{x} are not expected to be independent Gaussian conditioned on \mathbf{y} , as assumed in Proposition 1. So, using β_{std}^N from (25) may not work well in practice. We thus propose a method to automatically determine the correct β_{std} in Section 3.2.

Scalar-Gaussian illustration. To illustrate the behavior of the previously described regularizers, we consider the simple scalar-Gaussian case, where the generator is $G_{\theta}(z, \mathbf{y}) = \mu + \sigma z$, with code $z \sim \mathcal{N}(0, 1)$ and parameters $\theta = [\mu, \sigma]^T$. In this case, the generated posterior is $p_{\hat{\mathbf{x}} | \mathbf{y}}(x | \mathbf{y}) = \mathcal{N}(x; \mu, \sigma^2)$, and we assume that the true posterior is $p_{\mathbf{x} | \mathbf{y}}(x | \mathbf{y}) = \mathcal{N}(x; \mu_0, \sigma_0^2)$ for some μ_0 and $\sigma_0 > 0$.

Figure 1(a) plots P -sample supervised-L2 loss $\mathcal{L}_{2,P}(\theta)$ from (9) versus θ for $P = 8$. The plot shows that the minimizing $\hat{\theta} = \arg \min_{\theta} \mathcal{L}_{2,P}(\theta)$ yields $\hat{\mu} = \mu_0$ and $\hat{\sigma} = 0$, which corresponds to mode collapse. Figure 1(b) plots P -sample supervised-L2 loss plus variance reward $\mathcal{L}_{2,\text{var},P}(\theta, \beta_{\text{var}})$ from (14) versus θ for $\beta_{\text{var}} = 1/P$ and $P = 8$. This choice of β_{var} cancels the middle term in (11), which is responsible for mode collapse. As can be seen in Fig. 1(b), $\hat{\theta} = \arg \min_{\theta} \mathcal{L}_{2,\text{var},P}(\theta, \beta_{\text{var}})$ is no longer unique, and there is no incentive for mode collapse (i.e., $\hat{\sigma} = 0$) but no incentive to match the true posterior (i.e., $\hat{\sigma} = \sigma_0$). Figure 1(c) plots P -sample supervised-L1 loss plus std reward $\mathcal{L}_{1,\text{std},P}(\theta, \beta_{\text{std}})$ versus θ from (22) for $\beta_{\text{std}} = \beta_{\text{std}}^N$ from (25) and $P = 8$. The plots shows that $\hat{\theta} = \arg \min_{\theta} \mathcal{L}_{1,\text{std},P}(\theta, \beta_{\text{std}})$ recovers the true parameters (i.e., $\hat{\theta} = [\mu_0, \sigma_0]^T$) as predicted by Proposition 1. Finally, Figure 1(d) repeats the experiment from Figure 1(c), but with $P = 2$. The plot shows $\hat{\theta} = [\mu_0, \sigma_0]^T$ as predicted by Proposition 1. But, comparing Figure 1(d) to Figure 1(c), we can see that the cost surface becomes steeper for smaller P , i.e., the regularization becomes stronger. In real-world experiments, we find that $\mathcal{L}_{1,\text{std},P}(\theta, \beta_{\text{std}})$ -regularized cGANs work best when trained with the minimum value of $P = 2$.

3.2. Autotuning of β_{std}

We now propose a method to autotune β_{std} in (22) for a given training dataset. Our approach is inspired by the observation that larger values of β_{std} tend to yield samples $\hat{\mathbf{x}}_i$ with more variation. But more variation is not necessarily better; we want samples with the correct amount of variation. To assess variation, we will compare the expected ℓ_2 error of the P -sample average $\hat{\mathbf{x}}_{(P)}$ to that of $\hat{\mathbf{x}}_{(1)}$. In the case of mode collapse, these errors are identical. But when $\{\hat{\mathbf{x}}_i\}$

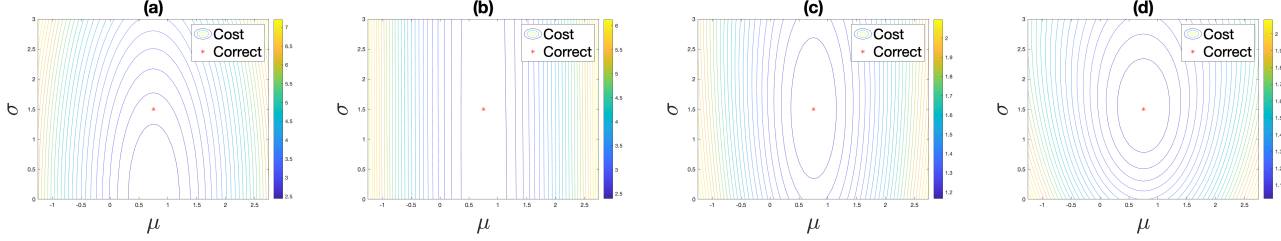


Figure 1. Scalar-Gaussian illustration of four different regularizers: (a) supervised-L2 at $P = 8$, (b) supervised-L2 plus variance reward with $\beta_{\text{var}} = 1/P$ at $P = 8$, (c) supervised-L1 plus std reward with $\beta_{\text{std}} = \beta_{\text{std}}^{\mathcal{N}}$ at $P = 8$, (d) supervised-L1 plus std reward with $\beta_{\text{std}} = \beta_{\text{std}}^{\mathcal{N}}$ at $P = 2$. The cost contours show the regularization value versus $\theta = [\mu, \sigma]^T$, and the red star shows the true posterior parameters $[\mu_0, \sigma_0]^T$. Subplot (a) shows that supervised-L2 promotes mode collapse (i.e., $\hat{\sigma} = 0$). Subplot (b) shows that adding a variance reward to supervised-L2 discourages mode collapse but does not recover the true parameters $[\mu_0, \sigma_0]^T$. Subplots (c)-(d) show that supervised-L1 plus std reward recovers the true parameters $[\mu_0, \sigma_0]^T$ for any $P \geq 2$. Comparing subplots (c) and (d), a smaller P yields a stronger effect.

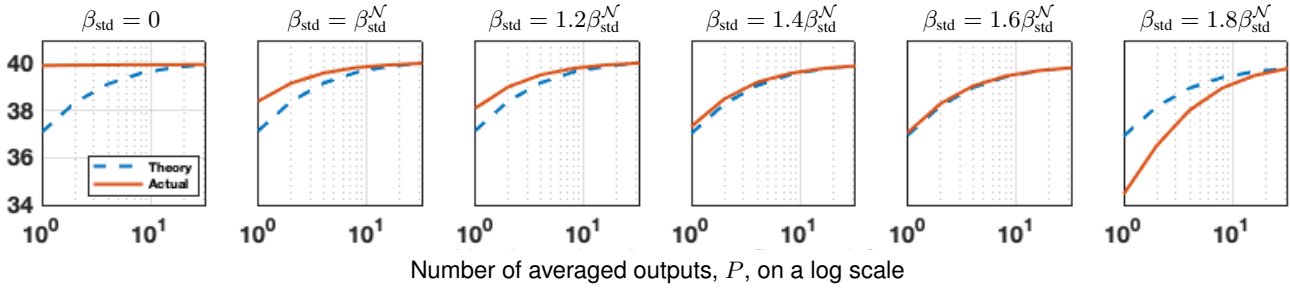


Figure 2. Example PSNR of $\hat{\mathbf{x}}_{(P)}$ versus P , the number of averaged outputs, for several values of β_{std} used during training. Also shown is the theoretical behavior for true-posterior samples.

are true posterior samples, these errors follow a particular relationship:

Proposition 2. Given generator outputs $\{\hat{\mathbf{x}}_i\}$ and their P -sample average $\hat{\mathbf{x}}_{(P)} \triangleq \frac{1}{P} \sum_{i=1}^P \hat{\mathbf{x}}_i$, let us define the expected ℓ_2 error on $\hat{\mathbf{x}}_{(P)}$ as

$$\mathcal{E}_P \triangleq \mathbb{E}\{\|\hat{\mathbf{x}}_{(P)} - \mathbf{x}\|_2^2 | \mathbf{y}\}. \quad (27)$$

If $\{\hat{\mathbf{x}}_i\}$ are independent samples of the true posterior (i.e., $\hat{\mathbf{x}}_i \sim p_{\mathbf{x}|\mathbf{y}}(\cdot | \mathbf{y})$), then

$$\mathcal{E}_P = \frac{P+1}{P} \mathcal{E}_{\text{mmse}} \quad \text{and so} \quad \frac{\mathcal{E}_P}{\mathcal{E}_1} = \frac{P+1}{2P}. \quad (28)$$

Proof. See Appendix D. \square

Figure 2 shows that, for any $P \geq 2$, $\mathcal{E}_P/\mathcal{E}_1$ grows with β_{std} . Together, Proposition 2 and Fig. 2 suggest to adjust β_{std} so that $\mathcal{E}_P/\mathcal{E}_1$ ratio obeys (28). In practice, at each epoch t , we approximate \mathcal{E}_P and \mathcal{E}_1 using a validation pair $(\mathbf{x}_t, \mathbf{y}_t)$ as follows:

$$\hat{\mathcal{E}}_{P,t} \triangleq \left\| \frac{1}{P} \sum_{i=1}^P G_{\theta}(\mathbf{z}_{i,t}, \mathbf{y}_t) - \mathbf{x}_t \right\|_2^2 \quad (29)$$

$$\hat{\mathcal{E}}_{1,t} \triangleq \|G_{\theta}(\mathbf{z}_{1,t}, \mathbf{y}_t) - \mathbf{x}_t\|_2^2, \quad (30)$$

where i.i.d. codes $\{\mathbf{z}_{i,t}\}_{i=1}^P$ are drawn independently of \mathbf{x}_t and \mathbf{y}_t . We then update β_{std} using gradient descent:

$$\beta_{\text{std},t+1} = \beta_{\text{std},t} - \mu_{\text{std}} \left(\left[\frac{P+1}{2P} \right]_{\text{dB}} - \left[\frac{\hat{\mathcal{E}}_{P,t}}{\hat{\mathcal{E}}_{1,t}} \right]_{\text{dB}} \right) \beta_{\text{std}}^{\mathcal{N}} \quad (31)$$

with $\beta_{\text{std},0} = \beta_{\text{std}}^{\mathcal{N}}$, some $\mu_{\text{std}} > 0$, and $[x]_{\text{dB}} \triangleq 10 \log_{10}(x)$.

3.3. Enforcing data consistency

In this section we describe a data-consistency procedure that can be optionally used with our cGAN. The motivation is that, in some applications such as medical imaging or inpainting, the end user may feel comfortable knowing that all generated reconstructions $\hat{\mathbf{x}}_i$ of \mathbf{x} from $\mathbf{y} = \mathbf{A}\mathbf{x} + \mathbf{w}$ (recall (1)) are consistent with the measurements in that

$$\mathbf{y} = \mathbf{A}\hat{\mathbf{x}}_i. \quad (32)$$

In this case, the recovery method aims only to restore the information about \mathbf{x} that was lost through the measurement process (i.e., the components of \mathbf{x} lying in the nullspace of \mathbf{A}) and so of course this approach only applies when \mathbf{A} has a non-trivial nullspace. Also, because no attempt is made to remove the noise \mathbf{w} in \mathbf{y} , this approach is appropriate only for high-SNR applications.

The proposed data-consistency approach leverages the fact that, if (32) holds, then $\mathbf{A}^+ \mathbf{y} = \mathbf{A}^+ \mathbf{A} \hat{\mathbf{x}}_i$ must also hold, where $(\cdot)^+$ denotes the pseudo-inverse. The quantity $\mathbf{A}^+ \mathbf{A}$ can be recognized as the orthogonal projection matrix associated with the row space of \mathbf{A} . So, (32) says that the components of $\hat{\mathbf{x}}_i$ in the row space of \mathbf{A} must equal $\mathbf{A}^+ \mathbf{y}$ while the components in the null space are unconstrained.

This implies the following data-consistency procedure:

$$\hat{\mathbf{x}}_i = (\mathbf{I} - \mathbf{A}^+ \mathbf{A}) \hat{\mathbf{x}}_i^{\text{raw}} + \mathbf{A}^+ \mathbf{y}. \quad (33)$$

where $\hat{\mathbf{x}}_i^{\text{raw}}$ is the raw generator output.

4. Numerical experiments

4.1. MRI

Data. In the MRI version of (1), \mathbf{x} is a complex-valued multicoil image (see Appendix F for more details). For the training $\{\mathbf{x}_t\}$, we used the first 8 slices of all fastMRI [36] T2 brain training volumes with at least 8 coils, cropping them to 384×384 pixels and compressing to 8 virtual coils [38], yielding 12 200 training images. Then 2376 testing and 784 validation images were obtained in the same manner from the fastMRI T2 brain testing volumes. From the 2376 testing images, we randomly selected 72 from which to compute performance metrics, in order to limit the evaluation time of our Langevin competitor [11] to roughly 6 days. To create measurement data \mathbf{y}_t , we transformed \mathbf{x}_t to the Fourier domain, sampled using the pseudo-random GRO pattern [2] at acceleration $R = 4$, and transformed the zero-filled k-space measurements back to the (complex, multicoil) image domain.

Architecture. We used a U-Net [22] for the generator and a standard CNN for the discriminator (see Appendix G for more details). The discriminator was patch-based [9] since that gave slightly improved performance. Also, we used the data-consistency processing from Section 3.3.

Training. At each training iteration, the generator takes in n_{batch} measurement samples \mathbf{y}_t , and P code vectors for every \mathbf{y}_t , and performs an optimization step on the loss

$$\mathcal{L}_G(\boldsymbol{\theta}) \triangleq \beta_{\text{adv}} \mathcal{L}_{\text{adv}}(\boldsymbol{\theta}, \boldsymbol{\phi}) + \mathcal{L}_{1,P}(\boldsymbol{\theta}) - \beta_{\text{std}} \mathcal{L}_{\text{std},P}(\boldsymbol{\theta}), \quad (34)$$

where by default we used $\beta_{\text{adv}} = 1\text{e-}2$, $n_{\text{batch}} = 40$, $P = 2$, and updated β_{std} according to (31). The discriminator then takes in the $P n_{\text{batch}}$ generator outputs and performs an optimization step on the loss

$$\mathcal{L}_D(\boldsymbol{\phi}) = -\mathcal{L}_{\text{adv}}(\boldsymbol{\theta}, \boldsymbol{\phi}) + \alpha_1 \mathcal{L}_{\text{gp}}(\boldsymbol{\phi}) + \alpha_2 \mathcal{L}_{\text{drift}}(\boldsymbol{\phi}), \quad (35)$$

where \mathcal{L}_{gp} is the gradient penalty from [7], $\mathcal{L}_{\text{drift}}$ is the drift penalty from [12], and $\alpha_1 = 10$ and $\alpha_2 = 0.001$ from [12]. We used one discriminator update per generator update [12]. The models were trained for 100 epochs using the Adam optimizer [14] with a learning rate of $1\text{e-}3$, $\beta_1 = 0$, and $\beta_2 = 0.99$, as in [12]. Running PyTorch on a server with 4 Tesla A100 GPUs, each with 82 GB of memory, the training of an MRI cGAN took approximately 2.5 days.

Validation/Testing. To evaluate performance, we converted the multicoil generator outputs to complex-valued images

using SENSE-based coil combining [20] with ESPIRiT-estimated [32] coil sensitivity maps (via SigPy [19]) as described in Appendix F. We then converted the images to the magnitude domain before computing FID, CFID, PSNR, SSIM, and average pixel-wise standard deviation (APSD), defined as $(\frac{1}{N^P} \sum_{i=1}^P \|\hat{\mathbf{x}}_{(P)} - \hat{\mathbf{x}}_i\|^2)^{1/2}$. PSNR and SSIM were computed from the P -averaged outputs $\hat{\mathbf{x}}_{(P)}$ (recall (12)), while FID and CFID were computed from the un-averaged outputs $\hat{\mathbf{x}}_i$. We used $P = 8$ for validation and $P = 32$ for testing, and computed FID and CFID using VGG-16 (not Inception-v3) for better agreement with radiologist’s perceptions [13].

Competitors. We compare our cGAN to Adler et al.’s cGAN [1], Ohayon et al.’s cGAN [17], and the fastMRI Langevin approach from Jalal et al. [11]. The cGAN from [1] uses generator loss $\beta_{\text{adv}} \mathcal{L}_{\text{adv}}^{\text{adler}}(\boldsymbol{\theta}, \boldsymbol{\phi})$ and discriminator loss $-\mathcal{L}_{\text{adv}}^{\text{adler}}(\boldsymbol{\theta}, \boldsymbol{\phi}) + \alpha_1 \mathcal{L}_{\text{gp}}(\boldsymbol{\phi}) + \alpha_2 \mathcal{L}_{\text{drift}}(\boldsymbol{\phi})$, while the cGAN from [17] uses generator loss $\beta_{\text{adv}} \mathcal{L}_{\text{adv}}(\boldsymbol{\theta}, \boldsymbol{\phi}) + \mathcal{L}_{2,P}(\boldsymbol{\theta})$ and discriminator loss $-\mathcal{L}_{\text{adv}}(\boldsymbol{\theta}, \boldsymbol{\phi}) + \alpha_1 \mathcal{L}_{\text{gp}}(\boldsymbol{\phi}) + \alpha_2 \mathcal{L}_{\text{drift}}(\boldsymbol{\phi})$, where for each we used the value of β_{adv} from the original paper. All cGANs used the same generator and discriminator architectures, except that [1] used extra discriminator input channels to facilitate the 3-input loss (7). For the Langevin approach [11], we did not modify the authors’ implementation from [10] except for the undersampling mask.

Reconstruction results. Table 1 shows performance results and evaluation time (for 4 samples). CFID, FID, PSNR, SSIM, APSD were evaluated on the 72 test images for comparison to the Langevin method. CFID was also evaluated on all 2376 test images, and again on all 14 576 training and test images, since using more samples reduces bias [26]. Our approach gave significantly better CFID and FID than the competitors. It also gave the highest PSNR and SSIM, although they were within one standard error of those from Ohayon et al.’s cGAN. We don’t consider APSD as a performance metric, but we note that Ohayon et al.’s APSD was almost two orders of magnitude lower than those of the other approaches, indicating mode collapse. The cGANs generated samples 3800 times faster than the Langevin approach.

Figure 3 shows example test-image reconstructions for the four different methods under test, along with the corresponding pixel-wise absolute errors $|\hat{\mathbf{x}}_{(P)} - \mathbf{x}|$ and pixel-wise standard deviations $(\frac{1}{P} \sum_{i=1}^P (\hat{\mathbf{x}}_{(P)} - \hat{\mathbf{x}}_i)^2)^{1/2}$. The mode collapse of Ohayon et al.’s cGAN is evident from the dark pixel-wise standard deviation image. The fact that the cGAN errors are less than the Langevin errors near the image corners is a consequence of minor differences in sensitivity-map estimation relative to [10]. Appendix H shows several other test-image reconstructions.

β_{std} autotuning results. Fig. 4 shows the difference between the P -sample PSNR gain $[\frac{\hat{\mathcal{E}}_{P,t}}{\hat{\mathcal{E}}_{1,t}}]_{\text{dB}}$ and the theoretical value $[\frac{P+1}{2P}]_{\text{dB}}$ versus the training epoch t for $P = 8$, as used

Table 1. Average results for $R = 4$ MRI reconstruction of 384×384 T2 brain images. \pm shows standard error. CFID¹, FID, PSNR, SSIM, and APSD used 72 test samples and $P = 32$. CFID² used 2376 test samples and $P = 8$. CFID³ used all 14 576 samples and $P = 1$.

Model	CFID ¹ ↓	CFID ² ↓	CFID ³ ↓	FID↓	PSNR↑	SSIM↑	APSD	Time (4)↓
Langevin (Jalal et al. [11])	5.29	-	-	6.12	37.88 ± 0.41	0.9042 ± 0.0062	5.9e-6	14 min
cGAN (Adler et al. [1])	3.76	3.27	2.95	5.82	37.17 ± 0.22	0.9360 ± 0.0037	3.7e-6	217 ms
cGAN (Ohayon et al. [17])	6.20	4.27	3.82	6.54	39.03 ± 0.29	0.9435 ± 0.0038	6.7e-8	217 ms
cGAN (Ours)	3.05	1.54	1.29	4.29	39.31 ± 0.29	0.9457 ± 0.0036	3.7e-6	217 ms

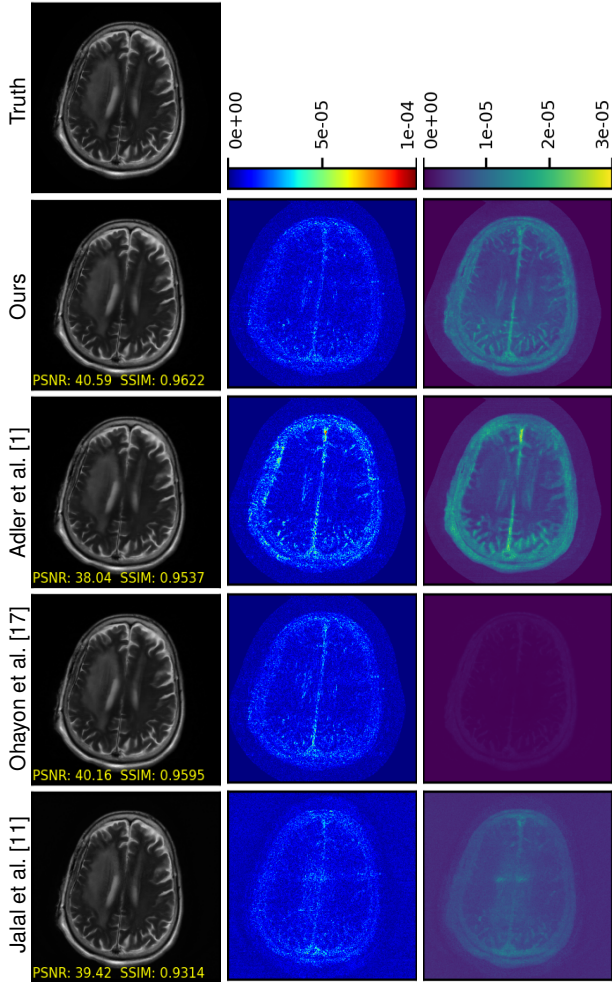


Figure 3. MRI reconstruction of a test image. Column one: reconstruction $\hat{x}_{(P)}$, two: pixel-wise absolute error $|\hat{x}_{(P)} - \mathbf{x}|$, three: pixel-wise standard-deviation $(\frac{1}{P} \sum_{i=1}^P (\hat{x}_i - \hat{x}_{(P)})^2)^{1/2}$.

during validation. As discussed in Section 3.2, the observed P -sample PSNR gain $[\frac{\hat{\mathcal{E}}_{P,t}}{\hat{\mathcal{E}}_{1,t}}]_{\text{dB}}$ is dependent on β_{std} , which is adapted according to (31). Fig. 5 shows the PSNR of test $\hat{x}_{(P)}$ versus P after autotuning. The figure shows that the observed curve closely matches the theoretical curve corresponding to true-posterior samples.

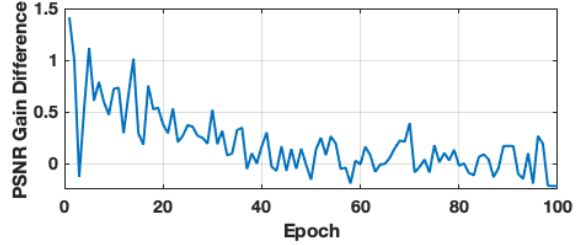


Figure 4. Difference between P -sample PSNR gain $[\frac{\hat{\mathcal{E}}_{P,t}}{\hat{\mathcal{E}}_{1,t}}]_{\text{dB}}$ and theoretical value $[\frac{P+1}{2P}]_{\text{dB}}$ versus training epoch t for $P = 8$.

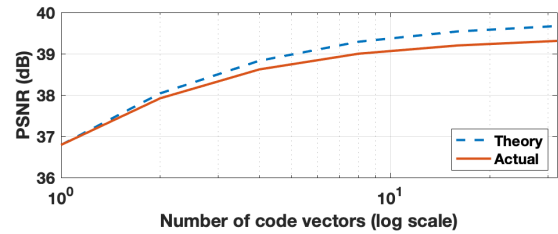


Figure 5. PSNR of $\hat{x}_{(P)}$ versus P after autotuning. Also shown is the theoretical behavior of samples from the true posterior.

4.2. Inpainting

Data. For our inpainting experiment, our objective was to complete the missing centered 64×64 square of an 128×128 CelebA-HQ face image [12]. We randomly split the dataset, yielding 27 000 images for training, 2000 for validation, and 1000 for testing. This application is qualitatively different from MR image recovery in that we don’t aim to recover the ground-truth image but rather hallucinate masked pixels that are consistent with the unmasked pixels.

Architecture. For our cGAN, we used the CoModGAN architecture from [41] along with our proposed $\mathcal{L}_{1,\text{std},P}$ regularization, but unlike the CoModGAN method we did not use MBSGD [12] at the discriminator.

Training/Validation/Testing. We use the same general training and testing procedure described in Section 4.1, but with $\beta_{\text{adv}} = 5e-3$, $n_{\text{batch}} = 128$, and 110 epochs of cGAN training. We didn’t compute PSNR or SSIM, since the goal is not to recover the original image but rather generate faces with high perceptual quality and diversity. Running PyTorch

Table 2. Average test results for inpainting a 64×64 centered square on a 128×128 celebA-HQ image. CFID¹ and FID used 1000 test images and $P = 32$, CFID² used 3000 test and validation images and $P = 8$, and CFID³ used all 30 000 images and $P = 1$.

Model	CFID ¹ ↓	CFID ² ↓	CFID ³ ↓	FID↓	Time (128)↓
Song et al. [27]	56.92	-	-	18.61	30 min
CoModGAN [41]	39.74	24.26	4.94	7.52	144 ms
Ours	39.66	22.54	4.70	6.45	144 ms

on a server with 4 Tesla A100 GPUs, each with 82 GB of memory, the cGAN training took approximately 1.5 days.

Competitors. We compared with the state-of-the-art CoModGAN [41] and the Langevin approach from Song et al. [27]. For CoModGAN, we used the PyTorch implementation from [37]. CoModGAN differs from our cGAN only in its use of MBSB and lack of $\mathcal{L}_{1, \text{std}, P}$ regularization. For Song et al., we used the authors’ implementation from [28] after training their NCSNv2 model on the 128×128 celebA-HQ dataset using their `celeba.yml` configuration.

Reconstruction results. Table 2 shows the test CFID, FID, APSD, and evaluation time (for 128 samples). Regarding CFID and FID (both evaluated using Inception-v3), our approach gave a small improvement over CoModGAN and a large improvement over Song et al. The cGANs generated samples 12 500 times faster than the Langevin method.

Fig. 6 shows five generated samples for the three methods under test. There, the samples generated by our approach have fewer undesirable artifacts than those of Song et al. and more variation than those of CoModGAN (note the eyes, mouth, and eyebrows). Additional examples can be found in Appendix H, with similar behavior.

5. Conclusion

We proposed a novel regularization technique for cGANs which consists of supervised- ℓ_1 loss plus an appropriately weighted standard-deviation reward, i.e., $\mathcal{L}_{1, P}(\theta) - \beta_{\text{std}} \mathcal{L}_{\text{std}, P}(\theta)$. For the simple case of an independent Gaussian posterior, we showed that, with appropriate β_{std} , minimizing our regularization yields generator samples that agree with the true posterior samples in both mean and covariance. For practical data, we proposed a method to autotune β_{std} .

For multicoil MR reconstruction and large-scale image inpainting, experiments showed our proposed method (with appropriate choice of generator and discriminator architecture) outperforming state-of-the-art cGAN and Langevin competitors in CFID as well as in accuracy metrics like PSNR and SSIM (for MRI) and perceptual metrics like FID. Compared to the Langevin approaches, our method produced samples thousands of times faster.

One limitation of our current implementation is that our cGAN is trained for a specific \mathbf{A} in (1). As future work, we

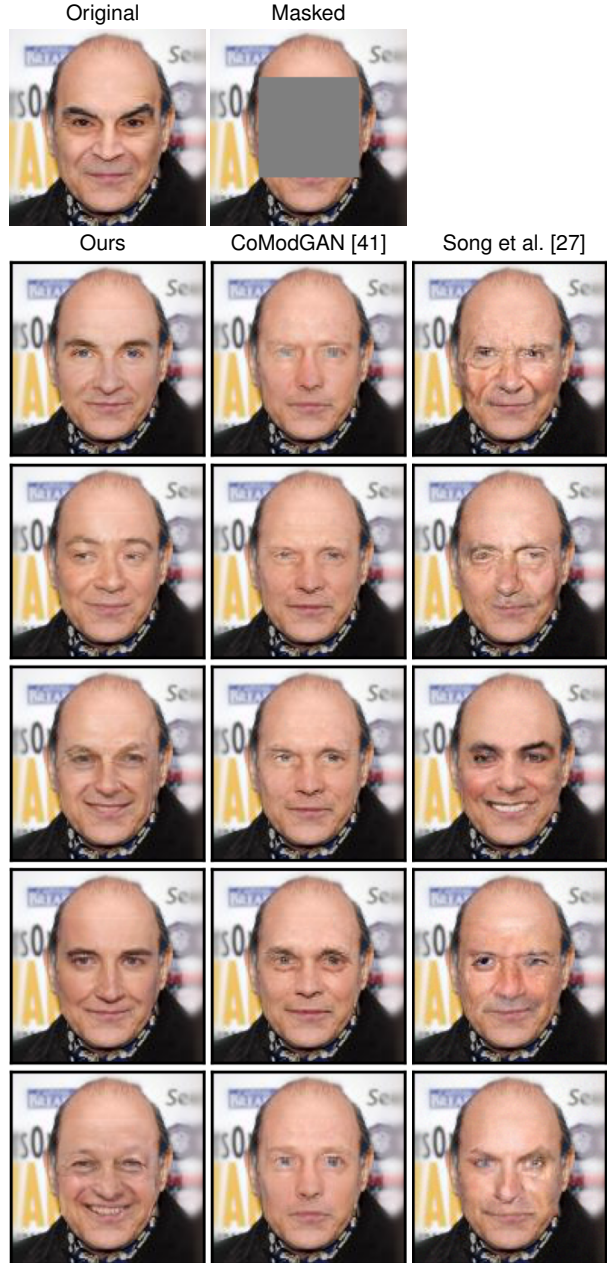


Figure 6. Example of inpainting a 64×64 centered square on an 128×128 resolution celebA-HQ test image.

plan to extend our approach so that it can handle a wide range of \mathbf{A} matrices. In the inpainting and MR applications, for example, our generator could take in both the measurements \mathbf{y} and the sampling mask. In addition, we plan to extend our approach to other applications, such as CT, superresolution, and deblurring.

References

- [1] Jonas Adler and Ozan Öktem. Deep Bayesian inversion. *arXiv:1811.05910*, 2018. 1, 2, 6, 7, 16, 17, 18, 19, 20, 21, 22
- [2] Rizwan Ahmad, Hui Xue, Shivraman Giri, Yu Ding, Jason Craft, and Orlando P. Simonetti. Variable density incoherent spatiotemporal acquisition (VISTA) for highly accelerated cardiac mri. *Magn. Reson. Med.*, 74, 2015. 6
- [3] Lynton Ardizzone, Carsten Lüth, Jakob Kruse, Carsten Rother, and Ullrich Köthe. Guided image generation with conditional invertible neural networks. *arXiv:1907.02392*, 2019. 1
- [4] Martin Arjovsky, Soumith Chintala, and Léon Bottou. Wasserstein generative adversarial networks. In *Proc. Int. Conf. Mach. Learn.*, volume 70, pages 214–223, Aug. 2017. 1, 2
- [5] Puneesh Deora, Bhavya Vasudeva, Saumik Bhattacharya, and Pyari Mohan Pradhan. Structure preserving compressive sensing MRI reconstruction using generative adversarial networks. In *Proc. IEEE Conf. Comp. Vision Pattern Recog. Workshop*, pages 2211–2219, June 2020. 16
- [6] Vineet Edupuganti, Morteza Mardani, Shreyas Vasanawala, and John Pauly. Uncertainty quantification in deep MRI reconstruction. *IEEE Trans. Med. Imag.*, 40(1):239–250, Jan. 2021. 1
- [7] Ishaan Gulrajani, Faruk Ahmed, Martin Arjovsky, Vincent Dumoulin, and Aaron Courville. Improved training of Wasserstein GANs. In *Proc. Neural Inf. Process. Syst. Conf.*, page 5769–5779, 2017. 1, 2, 6
- [8] Martin Heusel, Hubert Ramsauer, Thomas Unterthiner, Bernhard Nessler, and Sepp Hochreiter. GANs trained by a two time-scale update rule converge to a local Nash equilibrium. In *Proc. Neural Inf. Process. Syst. Conf.*, volume 30, 2017. 1, 3
- [9] Phillip Isola, Jun-Yan Zhu, Tinghui Zhou, and Alexei A Efros. Image-to-image translation with conditional adversarial networks. In *Proc. IEEE Conf. Comp. Vision Pattern Recog.*, pages 1125–1134, 2017. 1, 2, 4, 6, 16
- [10] Ajil Jalal, Marius Arvinte, Giannis Daras, Eric Price, Alex Dimakis, and Jonathan Tamir. csgm-mri-langevin. <https://github.com/utcsilab/csgm-mri-langevin>. Accessed: 2021-12-05. 6, 16
- [11] Ajil Jalal, Marius Arvinte, Giannis Daras, Eric Price, Alex Dimakis, and Jonathan Tamir. Robust compressed sensing MRI with deep generative priors. In *Proc. Neural Inf. Process. Syst. Conf.*, 2021. 1, 6, 7, 16, 18, 19, 20, 21, 22
- [12] Tero Karras, Timo Aila, Samuli Laine, and Jaakko Lehtinen. Progressive growing of GANs for improved quality, stability, and variation. In *Proc. Int. Conf. on Learn. Rep.*, 2018. 2, 6, 7
- [13] Segrey Kastruyulin, Jamil Zakirov, Nicola Pezzotti, and Dmitry V. Dylov. Image quality assessment for magnetic resonance imaging. *arXiv:2203.07809*, 2022. 6, 15
- [14] Diederik P. Kingma and Jimmy Ba. Adam: A method for stochastic optimization. In *Proc. Int. Conf. on Learn. Rep.*, 2015. 6
- [15] Fred C Leone, Lloyd S Nelson, and RB Nottingham. The folded normal distribution. *Technometrics*, 3(4):543–550, 1961. 12, 13
- [16] Luke Metz, Ben Poole, David Pfau, and Jascha Sohl-Dickstein. Unrolled generative adversarial networks. In *Proc. Int. Conf. on Learn. Rep.*, 2016. 2
- [17] Guy Ohayon, Theo Adrai, Gregory Vaksman, Michael Elad, and Peyman Milanfar. High perceptual quality image denoising with a posterior sampling CGAN. In *Proc. IEEE Int. Conf. Comput. Vis. Workshops*, volume 10, pages 1805–1813, 2021. 1, 2, 6, 7, 17, 18, 19, 20, 21, 22
- [18] Guy Ohayon, Theo Adrai, Gregory Vaksman, Michael Elad, and Peyman Milanfar. High perceptual quality image denoising with a posterior sampling cgan. Downloaded from <https://github.com/theoad/pscgan>, July 2021. 2
- [19] Frank Ong and Michael Lustig. SigPy: A python package for high performance iterative reconstruction. In *Proc. Annu. Meeting ISMRM*, volume 4819, 2019. 6
- [20] Klaas P. Pruessmann, Markus Weiger, Markus B. Scheidegger, and Peter Boesiger. SENSE: Sensitivity encoding for fast MRI. *Magn. Reson. Med.*, 42(5):952–962, 1999. 6, 15
- [21] Alec Radford, Luke Metz, and Soumith Chintala. Unsupervised representation learning with deep convolutional generative adversarial networks. *arXiv:1511.06434*, 2015. 2
- [22] Olaf Ronneberger, Philipp Fischer, and Thomas Brox. U-Net: Convolutional networks for biomedical image segmentation. In *Proc. Intl. Conf. Med. Image Comput. Comput. Assist. Intervent.*, pages 234–241, 2015. 6, 16
- [23] Tim Salimans, Ian Goodfellow, Wojciech Zaremba, Vicki Cheung, Alec Radford, and Xi Chen. Improved techniques for training GANs. In *Proc. Neural Inf. Process. Syst. Conf.*, volume 29, 2016. 2
- [24] Karen Simonyan and Andrew Zisserman. Very deep convolutional networks for large-scale image recognition. *arXiv:1409.1556*, 2014. 15

- [25] Kihyuk Sohn, Honglak Lee, and Xinchun Yan. Learning structured output representation using deep conditional generative models. In *Proc. Neural Inf. Process. Syst. Conf.*, 2015. 1
- [26] Michael Soloveitchik, Tzvi Diskin, Efrat Morin, and Ami Wiesel. Conditional Frechet inception distance. *arXiv:2103.11521*, 2021. 1, 3, 6, 14, 15, 17
- [27] Yang Song and Stefano Ermon. Improved techniques for training score-based generative models. In *Proc. Neural Inf. Process. Syst. Conf.*, 2020. 1, 8, 16, 23, 24, 25, 26
- [28] Yang Song and Stefano Ermon. Improved techniques for training score-based generative models. Downloaded from <https://github.com/ermongroup/ncsnv2/tree/1bcea03bd97d76a8357b9d674fa0bae5ff0f1093>, Oct. 2022. 8, 16
- [29] He Sun and Katherine L Bouman. Deep probabilistic imaging: Uncertainty quantification and multi-modal solution characterization for computational imaging. In *Proc. AAAI Conf. Artificial Intell.*, volume 35, pages 2628–2637, 2021. 1
- [30] Christian Szegedy, Vincent Vanhoucke, Sergey Ioffe, Jon Shlens, and Zbigniew Wojna. Rethinking the inception architecture for computer vision. In *Proc. IEEE Conf. Comp. Vision Pattern Recog.*, 2016. 3, 15
- [31] Francesco Tonolini, Jack Radford, Alex Turpin, Daniele Faccio, and Roderick Murray-Smith. Variational inference for computational imaging inverse problems. *J. Mach. Learn. Res.*, 21(179):1–46, 2020. 1
- [32] Martin Uecker, Peng Lai, Mark J Murphy, Patrick Virtue, Michael Elad, John M Pauly, Shreyas S Vasanaawala, and Michael Lustig. ESPIRiT—an eigenvalue approach to autocalibrating parallel MRI: Where SENSE meets GRAPPA. *Magn. Reson. Med.*, 71(3):990–1001, 2014. 6, 15
- [33] Zhou Wang, Alan C Bovik, Hamid R Sheikh, and Eero P Simoncelli. Image quality assessment: From error visibility to structural similarity. *IEEE Trans. Image Process.*, 13(4):600–612, Apr. 2004. 1
- [34] Max Welling and Yee W Teh. Bayesian learning via stochastic gradient Langevin dynamics. In *Proc. Int. Conf. Mach. Learn.*, pages 681–688, 2011. 1
- [35] Christina Winkler, Daniel Worrall, Emiel Hoogeboom, and Max Welling. Learning likelihoods with conditional normalizing flows. *arXiv preprint arXiv:1912.00042*, 2019. 1
- [36] Jure Zbontar, Florian Knoll, Anuroop Sriram, Matthew J. Muckley, Mary Bruno, Aaron Defazio, Marc Parente, Krzysztof J. Geras, Joe Katsnelson, Hersh Chandarana, Zizhao Zhang, Michal Drozdal, Adriana Romero, Michael Rabbat, Pascal Vincent, James Pinkerton, Duo Wang, Nafissa Yakubova, Erich Owens, C. Lawrence Zitnick, Michael P. Recht, Daniel K. Sodickson, and Yvonne W. Lui. fastMRI: An open dataset and benchmarks for accelerated MRI. *arXiv:1811.08839*, 2018. 6, 15
- [37] Yu Zeng. co-mod-gan-pytorch. Downloaded from <https://github.com/zengxianyu/co-mod-gan-pytorch>, Sept. 2022. 8, 16
- [38] Tao Zhang, John M Pauly, Shreyas S Vasanaawala, and Michael Lustig. Coil compression for accelerated imaging with Cartesian sampling. *Magn. Reson. Med.*, 69(2):571–582, 2013. 6
- [39] Hang Zhao, Orazio Gallo, Iuri Frosio, and Jan Kautz. Loss functions for image restoration with neural networks. *IEEE Trans. Comput. Imag.*, 3(1):47–57, Mar. 2017. 4
- [40] He Zhao, Huiqi Li, Sebastian Maurer-Stroh, and Li Cheng. Synthesizing retinal and neuronal images with generative adversarial nets. *Med. Image Analysis*, 49, 07 2018. 1, 4
- [41] Shengyu Zhao, Jonathan Cui, Yilun Sheng, Yue Dong, Xiao Liang, Eric I-Chao Chang, and Yan Xu. Large scale image completion via co-modulated generative adversarial networks. In *Proc. Int. Conf. on Learn. Rep.*, 2021. 1, 7, 8, 17, 23, 24, 25, 26

Supplementary Materials

A. Derivation of (11)

Using the definitions of $\widehat{\mathbf{x}}_{(P)}$, $\bar{\mathbf{x}}$, $\mathbf{d}_{(P)}$, $\widehat{\mathbf{x}}_{\text{mmse}}$, \mathbf{e}_{mmse} from (12), and leveraging the fact that $\widehat{\mathbf{x}}_{\text{mmse}}$ and $\bar{\mathbf{x}}$ are deterministic given \mathbf{y} , we can write the inner term in (10) as

$$\begin{aligned} & \mathbb{E}_{\mathbf{x}, \mathbf{z}_1, \dots, \mathbf{z}_P | \mathbf{y}} \{ \|\mathbf{x} - \widehat{\mathbf{x}}_{(P)}\|_2^2 | \mathbf{y} \} \\ &= \mathbb{E}_{\mathbf{x}, \mathbf{z}_1, \dots, \mathbf{z}_P | \mathbf{y}} \{ \|\widehat{\mathbf{x}}_{\text{mmse}} + \mathbf{e}_{\text{mmse}} - \bar{\mathbf{x}} - \mathbf{d}_{(P)}\|_2^2 | \mathbf{y} \} \end{aligned} \quad (\text{A.1})$$

$$\begin{aligned} &= \mathbb{E}_{\mathbf{x}, \mathbf{z}_1, \dots, \mathbf{z}_P | \mathbf{y}} \{ \|\widehat{\mathbf{x}}_{\text{mmse}} - \bar{\mathbf{x}}\|_2^2 | \mathbf{y} \} + 2 \operatorname{Re} \mathbb{E}_{\mathbf{x}, \mathbf{z}_1, \dots, \mathbf{z}_P | \mathbf{y}} \{ (\widehat{\mathbf{x}}_{\text{mmse}} - \bar{\mathbf{x}})^H (\mathbf{e}_{\text{mmse}} - \mathbf{d}_{(P)}) | \mathbf{y} \} + \mathbb{E}_{\mathbf{x}, \mathbf{z}_1, \dots, \mathbf{z}_P | \mathbf{y}} \{ \|\mathbf{e}_{\text{mmse}} - \mathbf{d}_{(P)}\|_2^2 | \mathbf{y} \} \\ &= \|\widehat{\mathbf{x}}_{\text{mmse}} - \bar{\mathbf{x}}\|_2^2 + 2 \operatorname{Re} \left[\underbrace{(\widehat{\mathbf{x}}_{\text{mmse}} - \bar{\mathbf{x}})^H \mathbb{E}_{\mathbf{x}, \mathbf{z}_1, \dots, \mathbf{z}_P | \mathbf{y}} \{ (\mathbf{e}_{\text{mmse}} - \mathbf{d}_{(P)}) | \mathbf{y} \}}_{= \mathbf{0}} \right] + \mathbb{E}_{\mathbf{x}, \mathbf{z}_1, \dots, \mathbf{z}_P | \mathbf{y}} \{ \|\mathbf{e}_{\text{mmse}} - \mathbf{d}_{(P)}\|_2^2 | \mathbf{y} \} \end{aligned} \quad (\text{A.2})$$

$$= \|\widehat{\mathbf{x}}_{\text{mmse}} - \bar{\mathbf{x}}\|_2^2 + \mathbb{E}_{\mathbf{x}, \mathbf{z}_1, \dots, \mathbf{z}_P | \mathbf{y}} \{ \|\mathbf{e}_{\text{mmse}} - \mathbf{d}_{(P)}\|_2^2 | \mathbf{y} \}. \quad (\text{A.3})$$

where in (A.2) we used the fact that $\mathbf{d}_{(P)}$ and \mathbf{e}_{mmse} are both zero-mean when conditioned on \mathbf{y} . Furthermore we can leverage the fact that $\{\mathbf{z}_i\}$ are independent of \mathbf{x} and \mathbf{y} to write

$$\begin{aligned} & \mathbb{E}_{\mathbf{x}, \mathbf{z}_1, \dots, \mathbf{z}_P | \mathbf{y}} \{ \|\mathbf{e}_{\text{mmse}} - \mathbf{d}_{(P)}\|_2^2 | \mathbf{y} \} \\ &= \mathbb{E}_{\mathbf{x}, \mathbf{z}_1, \dots, \mathbf{z}_P | \mathbf{y}} \{ \|\mathbf{e}_{\text{mmse}}\|_2^2 | \mathbf{y} \} + 2 \operatorname{Re} \mathbb{E}_{\mathbf{x}, \mathbf{z}_1, \dots, \mathbf{z}_P | \mathbf{y}} \{ \mathbf{e}_{\text{mmse}}^H \mathbf{d}_{(P)} | \mathbf{y} \} + \mathbb{E}_{\mathbf{x}, \mathbf{z}_1, \dots, \mathbf{z}_P | \mathbf{y}} \{ \|\mathbf{d}_{(P)}\|_2^2 | \mathbf{y} \} \end{aligned} \quad (\text{A.4})$$

$$= \mathbb{E}_{\mathbf{x} | \mathbf{y}} \{ \|\mathbf{e}_{\text{mmse}}\|_2^2 | \mathbf{y} \} + 2 \operatorname{Re} \left[\underbrace{\mathbb{E}_{\mathbf{x} | \mathbf{y}} \{ \mathbf{e}_{\text{mmse}} | \mathbf{y} \}}_{= \mathbf{0}} \right]^H \underbrace{\mathbb{E}_{\mathbf{z}_1, \dots, \mathbf{z}_P | \mathbf{y}} \{ \mathbf{d}_{(P)} | \mathbf{y} \}}_{= \mathbf{0}} + \mathbb{E}_{\mathbf{z}_1, \dots, \mathbf{z}_P | \mathbf{y}} \{ \|\mathbf{d}_{(P)}\|_2^2 | \mathbf{y} \}. \quad (\text{A.5})$$

Finally, we can leverage the fact that $\{\mathbf{z}_i\}$ are i.i.d. to write

$$\mathbb{E}_{\mathbf{z}_1, \dots, \mathbf{z}_P | \mathbf{y}} \{ \|\mathbf{d}_{(P)}\|_2^2 | \mathbf{y} \} = \mathbb{E}_{\mathbf{z}_1, \dots, \mathbf{z}_P | \mathbf{y}} \{ \|\frac{1}{P} \sum_{i=1}^P \mathbf{d}_i\|_2^2 | \mathbf{y} \} \quad (\text{A.6})$$

$$= \frac{1}{P^2} \sum_{i=1}^P \mathbb{E}_{\mathbf{z}_i | \mathbf{y}} \{ \|\mathbf{d}_i\|_2^2 | \mathbf{y} \} \quad (\text{A.7})$$

$$= \frac{1}{P} \mathbb{E}_{\mathbf{z}_i | \mathbf{y}} \{ \|\mathbf{d}_i\|_2^2 | \mathbf{y} \} \text{ for any } i. \quad (\text{A.8})$$

Combining (10), (A.3), (A.5), and (A.8), we get (11), i.e.,

$$\mathcal{L}_{2,P}(\boldsymbol{\theta}) = \mathbb{E}_{\mathbf{y}} \left\{ \|\widehat{\mathbf{x}}_{\text{mmse}} - \bar{\mathbf{x}}\|_2^2 + \frac{1}{P} \mathbb{E}_{\mathbf{z}_i | \mathbf{y}} \{ \|\mathbf{d}_i\|_2^2 | \mathbf{y} \} + \mathbb{E}_{\mathbf{x} | \mathbf{y}} \{ \|\mathbf{e}_{\text{mmse}}\|_2^2 | \mathbf{y} \} \right\}. \quad (\text{A.9})$$

B. Derivation of (16)

To show that the expression for $\mathcal{L}_{\text{var},P}$ from (16) holds, we first rewrite (15) as

$$\mathcal{L}_{\text{var},P}(\boldsymbol{\theta}) = \frac{1}{P-1} \sum_{i=1}^P \mathbb{E}_{\mathbf{y}} \{ \mathbb{E}_{\mathbf{z}_1, \dots, \mathbf{z}_P | \mathbf{y}} \{ \|\widehat{\mathbf{x}}_i - \widehat{\mathbf{x}}_{(P)}\|_2^2 | \mathbf{y} \} \} \quad (\text{B.1})$$

where the definitions in (12) imply

$$\mathbb{E}_{\mathbf{z}_1, \dots, \mathbf{z}_P | \mathbf{y}} \{ \|\widehat{\mathbf{x}}_i - \widehat{\mathbf{x}}_{(P)}\|_2^2 | \mathbf{y} \} = \mathbb{E}_{\mathbf{z}_1, \dots, \mathbf{z}_P | \mathbf{y}} \{ \|\bar{\mathbf{x}} + \mathbf{d}_i - \mathbf{d}_{(P)} - \bar{\mathbf{x}}\|_2^2 | \mathbf{y} \} \quad (\text{B.2})$$

$$= \mathbb{E}_{\mathbf{z}_1, \dots, \mathbf{z}_P | \mathbf{y}} \{ \|\mathbf{d}_i - \frac{1}{P} \sum_{j=1}^P \mathbf{d}_j\|_2^2 | \mathbf{y} \} \quad (\text{B.3})$$

$$= \mathbb{E}_{\mathbf{z}_1, \dots, \mathbf{z}_P | \mathbf{y}} \{ \|(1 - \frac{1}{P})\mathbf{d}_i - \frac{1}{P} \sum_{j \neq i} \mathbf{d}_j\|_2^2 | \mathbf{y} \} \quad (\text{B.4})$$

$$= (1 - \frac{1}{P})^2 \mathbb{E}_{\mathbf{z}_i | \mathbf{y}} \{ \|\mathbf{d}_i\|_2^2 | \mathbf{y} \} + \frac{P-1}{P^2} \mathbb{E}_{\mathbf{z}_i | \mathbf{y}} \{ \|\mathbf{d}_i\|_2^2 | \mathbf{y} \} \quad (\text{B.5})$$

$$= \frac{P-1}{P} \mathbb{E}_{\mathbf{z}_i | \mathbf{y}} \{ \|\mathbf{d}_i\|_2^2 | \mathbf{y} \} \text{ for any } i. \quad (\text{B.6})$$

For (B.5), we leveraged the zero-mean and i.i.d. nature of $\{\mathbf{e}_i\}$ conditioned on \mathbf{y} . By plugging (B.6) into (B.1), we get

$$\mathcal{L}_{\text{var},P}(\boldsymbol{\theta}) = \frac{1}{P} \sum_{i=1}^P \mathbb{E}_{\mathbf{y}} \{ \mathbb{E}_{\mathbf{z}_i | \mathbf{y}} \{ \|\mathbf{d}_i\|_2^2 | \mathbf{y} \} \} \quad (\text{B.7})$$

$$= \mathbb{E}_{\mathbf{y}} \{ \mathbb{E}_{\mathbf{z}_i | \mathbf{y}} \{ \|\mathbf{d}_i\|_2^2 | \mathbf{y} \} \} \text{ for any } i, \quad (\text{B.8})$$

where (B.8) follows because $\{\mathbf{d}_i\}$ are i.i.d. when conditioned on \mathbf{y} . Note that (B.8) equals the trace of the covariance of $\widehat{\mathbf{x}}_i$.

C. Proof of Proposition 1

Here we prove Proposition 1. To begin, we rewrite (23)-(24) as

$$\mathcal{L}_{1,P}(\boldsymbol{\theta}) = \sum_{j=1}^N \mathbb{E}_{\mathbf{y}} \left\{ \mathbb{E}_{\mathbf{x}, \mathbf{z}_1, \dots, \mathbf{z}_P | \mathbf{y}} \left\{ |x_j - \frac{1}{P} \sum_{i=1}^P \hat{x}_{ij}| \mid \mathbf{y} \right\} \right\} \quad (\text{C.1})$$

$$\mathcal{L}_{\text{std},P}(\boldsymbol{\theta}) = \sum_{j=1}^N \mathbb{E}_{\mathbf{y}} \left\{ \mathbb{E}_{\mathbf{z}_1, \dots, \mathbf{z}_P | \mathbf{y}} \left\{ \frac{\gamma_P}{P} \sum_{i=1}^P |\hat{x}_{ij} - \frac{1}{P} \sum_{k=1}^P \hat{x}_{kj}| \mid \mathbf{y} \right\} \right\}, \quad (\text{C.2})$$

where $x_j \triangleq [\mathbf{x}]_j$, $\hat{x}_{ij} \triangleq [\hat{\mathbf{x}}_i]_j$, and

$$\gamma_P \triangleq \sqrt{\frac{\pi P}{2(P-1)}}. \quad (\text{C.3})$$

To simplify the notation in the sequel, we will consider an arbitrary fixed value of j and use the abbreviations

$$x_j \rightarrow X, \quad \hat{x}_{ij} \rightarrow \hat{X}_i. \quad (\text{C.4})$$

Recall that \mathbf{x} and $\{\hat{\mathbf{x}}_i\}$ are mutually independent when conditioned on \mathbf{y} because the code vectors $\{\mathbf{z}_i\}$ are generated independently of both \mathbf{x} and \mathbf{y} . In the context of Proposition 1, we also assume that the vector elements x_j and \hat{x}_{ij} are independent Gaussian when conditioned on \mathbf{y} . This implies that we can make the notational shift

$$p_{\mathbf{x}|\mathbf{y}}(x_j|\mathbf{y}) \rightarrow \mathcal{N}(X; \mu_0, \sigma_0^2), \quad p_{\hat{\mathbf{x}}|\mathbf{y}}(\hat{x}_{ij}|\mathbf{y}) \rightarrow \mathcal{N}(\hat{X}_i; \mu, \sigma^2), \quad (\text{C.5})$$

where X and $\{\hat{X}_i\}$ are mutually independent. With this simplified notation, we note that $[\hat{\mathbf{x}}_{\text{mmse}}]_j \rightarrow \mu_0$, and that mode collapse corresponds to $\sigma = 0$.

Furthermore, if $\boldsymbol{\theta}$ can completely control the statistics of \hat{X}_i , which are now parameterized by (μ, σ) , then (26) can be rewritten as

$$(\mu_*, \sigma_*) = \arg \min_{\mu, \sigma} \left\{ \mathcal{L}_{1,P}(\mu, \sigma) - \beta_{\text{std}} \mathcal{L}_{\text{std},P}(\mu, \sigma) \right\} \Rightarrow \begin{cases} \mu_* = \mu_0 \\ \sigma_* = \sigma_0 \end{cases} \quad (\text{C.6})$$

with

$$\mathcal{L}_{1,P}(\mu, \sigma) = \mathbb{E}_{X, \hat{X}_1, \dots, \hat{X}_P} \left\{ |X - \frac{1}{P} \sum_{i=1}^P \hat{X}_i| \right\} \quad (\text{C.7})$$

$$\mathcal{L}_{\text{std},P}(\mu, \sigma) = \mathbb{E}_{\hat{X}_1, \dots, \hat{X}_P} \left\{ \frac{\gamma_P}{P} \sum_{i=1}^P |\hat{X}_i - \frac{1}{P} \sum_{k=1}^P \hat{X}_k| \right\}. \quad (\text{C.8})$$

Although σ_* must be positive, it turns out that we do not need to enforce this in the optimization because it will arise naturally.

To further analyze (C.7) and (C.8), we define

$$\hat{\mu} \triangleq \frac{1}{P} \sum_{i=1}^P \hat{X}_i \quad (\text{C.9})$$

$$\hat{\sigma} \triangleq \frac{\gamma_P}{P} \sum_{i=1}^P |\hat{X}_i - \hat{\mu}|. \quad (\text{C.10})$$

The quantity $\hat{\mu}$ can be recognized as the unbiased estimate of the mean μ of \hat{X}_i , and we now show that $\hat{\sigma}$ is an unbiased estimate of the standard-deviation σ of \hat{X}_i in the case of Gaussian \hat{X}_i . To see this, first observe that the i.i.d. $\mathcal{N}(\mu, \sigma^2)$ property of $\{\hat{X}_i\}$ implies that $\hat{X}_i - \hat{\mu} = (1 - \frac{1}{P})\hat{X}_i - \frac{1}{P} \sum_{k \neq i} \hat{X}_k$ is Gaussian with mean zero and variance $(1 - \frac{1}{P})^2 \sigma^2 + \frac{P-1}{P^2} \sigma^2 = \frac{P-1}{P} \sigma^2$.

The variable $|\hat{X}_i - \hat{\mu}|$ is thus half-normal distributed [15] with mean $\sqrt{\frac{2(P-1)}{\pi P}} \sigma$. Because $\{\hat{X}_i\}$ are i.i.d., the variable $\frac{1}{P} \sum_{i=1}^P |\hat{X}_i - \hat{\mu}|$ inherits the same mean. Finally, multiplying that variable by γ_P yields $\hat{\sigma}$ from (C.10), and multiplying its mean using the expression for γ_P from (C.3) implies

$$\mathbb{E}\{\hat{\sigma}\} = \sigma, \quad (\text{C.11})$$

and so $\hat{\sigma}$ is an unbiased estimator of σ , the standard deviation of \hat{X}_i .

With the above definitions of $\hat{\mu}$ and $\hat{\sigma}$, the optimization cost in (C.6) can be written as

$$\mathcal{L}_{1,P}(\mu, \sigma) - \beta_{\text{std}} \mathcal{L}_{\text{std},P}(\mu, \sigma) = \mathbb{E}_{X, \hat{X}_1, \dots, \hat{X}_P} \left\{ |X - \hat{\mu}| \right\} - \beta_{\text{std}} \mathbb{E}_{\hat{X}_1, \dots, \hat{X}_P} \left\{ \hat{\sigma} \right\} \quad (\text{C.12})$$

$$= \mathbb{E}_{X, \hat{X}_1, \dots, \hat{X}_P} \left\{ |X - \hat{\mu}| \right\} - \beta_{\text{std}} \sigma, \quad (\text{C.13})$$

where in the last step we exploited the unbiased property of $\hat{\sigma}$. To proceed further, we note that under the i.i.d. Gaussian assumption on $\{\hat{X}_i\}$ we get $\hat{\mu} \sim \mathcal{N}(\mu, \sigma^2/P)$, after which the mutual independence of $\{\hat{X}_i\}$ and X yields

$$X - \hat{\mu} \sim \mathcal{N}(\mu_0 - \mu, \sigma_0^2 + \sigma^2/P). \quad (\text{C.14})$$

Taking the absolute value of a Gaussian random yields a folded-normal random variable [15]. Using the mean and variance in (C.14), the expressions in [15] yield

$$\mathbb{E}_{X, \hat{X}_1, \dots, \hat{X}_P} \{|X - \hat{\mu}|\} = \sqrt{\frac{2(\sigma_0^2 + \sigma^2/P)}{\pi}} \exp\left(-\frac{(\mu_0 - \mu)^2}{2(\sigma_0^2 + \sigma^2/P)}\right) + (\mu_0 - \mu) \operatorname{erf}\left(\frac{\mu_0 - \mu}{\sqrt{2(\sigma_0^2 + \sigma^2/P)}}\right). \quad (\text{C.15})$$

Thus the optimization cost (C.13) can be written as

$$J(\mu, \sigma) \triangleq \sqrt{\frac{2(\sigma_0^2 + \sigma^2/P)}{\pi}} \exp\left(-\frac{(\mu - \mu_0)^2}{2(\sigma_0^2 + \sigma^2/P)}\right) + (\mu - \mu_0) \operatorname{erf}\left(\frac{\mu - \mu_0}{\sqrt{2(\sigma_0^2 + \sigma^2/P)}}\right) - \beta_{\text{std}}\sigma. \quad (\text{C.16})$$

Since $J(\cdot, \cdot)$ is convex, the minimizer $(\mu_*, \sigma_*) = \arg \min_{\mu, \sigma} J(\mu, \sigma)$ satisfies $\nabla J(\mu_*, \sigma_*) = (0, 0)$. To streamline the derivation, we define

$$c \triangleq \sqrt{2(\sigma_0^2 + \sigma^2/P)/\pi}, \quad s \triangleq \sqrt{\sigma_0^2 + \sigma^2/P} \quad (\text{C.17})$$

so that

$$J(\mu, \sigma) = c \exp\left(-\frac{(\mu - \mu_0)^2}{2s^2}\right) + (\mu - \mu_0) \operatorname{erf}\left(\frac{\mu - \mu_0}{\sqrt{2}s^2}\right) - \beta_{\text{std}}\sigma. \quad (\text{C.18})$$

Because c and s are invariant to μ , we get

$$\frac{\partial J(\mu, \sigma)}{\partial \mu} = -c \exp\left(-\frac{(\mu - \mu_0)^2}{2s^2}\right) \frac{\mu - \mu_0}{s^2} + \operatorname{erf}\left(\frac{\mu - \mu_0}{\sqrt{2}s^2}\right) + (\mu - \mu_0) \frac{2}{\sqrt{\pi}} \exp\left(-\frac{(\mu - \mu_0)^2}{2s^2}\right), \quad (\text{C.19})$$

which equals zero if and only if $\mu = \mu_0$. Thus we have determined that $\mu_* = \mu_0$. Plugging $\mu_* = \mu_0$ into (C.16), we find

$$J(\mu_*, \sigma) = \sqrt{2(\sigma_0^2 + \sigma^2/P)/\pi} - \beta_{\text{std}}\sigma. \quad (\text{C.20})$$

Taking the derivative with respect to σ , we get

$$\frac{\partial J(\mu_*, \sigma)}{\partial \sigma} = \sqrt{\frac{2}{\pi P(P\sigma_0^2/\sigma^2 + 1)}} - \beta_{\text{std}} \quad (\text{C.21})$$

$$= \sqrt{\frac{2}{\pi P(P\sigma_0^2/\sigma^2 + 1)}} - \sqrt{\frac{2}{\pi P(P + 1)}}, \quad (\text{C.22})$$

where in the last step we applied the value of β_{std} from (25). It can now be seen that $\frac{\partial J(\mu_*, \sigma)}{\partial \sigma} = 0$ if and only if $\sigma = \sigma_0$, which implies that $\sigma_* = \sigma_0$. Thus we have established (C.6), which completes the proof of Proposition 1.

D. Proof of Proposition 2

Here we prove Proposition 2. Recall from (12) that $\hat{\mathbf{x}}_{\text{mmse}} \triangleq \mathbb{E}\{\mathbf{x}|\mathbf{y}\}$. Let's define

$$\hat{\mathbf{e}}_i \triangleq \hat{\mathbf{x}}_i - \hat{\mathbf{x}}_{\text{mmse}} \quad (\text{D.1})$$

$$\mathbf{e} \triangleq \mathbf{x} - \hat{\mathbf{x}}_{\text{mmse}}. \quad (\text{D.2})$$

Then from (27),

$$\mathcal{E}_P = \mathbb{E}\{\|\hat{\mathbf{x}}_{(P)} - \mathbf{x}\|^2 | \mathbf{y}\} \quad (\text{D.3})$$

$$= \mathbb{E}\{\|(\frac{1}{P} \sum_{i=1}^P \hat{\mathbf{x}}_i) - \mathbf{x}\|^2 | \mathbf{y}\} \quad (\text{D.4})$$

$$= \mathbb{E}\{\|\frac{1}{P} \sum_{i=1}^P (\hat{\mathbf{x}}_i - \mathbf{x})\|^2 | \mathbf{y}\} \quad (\text{D.5})$$

$$= \frac{1}{P^2} \mathbb{E}\{\|\sum_{i=1}^P (\hat{\mathbf{x}}_i - \hat{\mathbf{x}}_{\text{mmse}} + \hat{\mathbf{x}}_{\text{mmse}} - \mathbf{x})\|^2 | \mathbf{y}\} \quad (\text{D.6})$$

$$= \frac{1}{P^2} \mathbb{E}\{\|\sum_{i=1}^P (\hat{\mathbf{e}}_i - \mathbf{e})\|^2 | \mathbf{y}\} \quad (\text{D.7})$$

$$= \frac{1}{P^2} \mathbb{E}\{\sum_{i=1}^P (\hat{\mathbf{e}}_i - \mathbf{e})^\top \sum_{j=1}^P (\hat{\mathbf{e}}_j - \mathbf{e}) | \mathbf{y}\} \quad (\text{D.8})$$

$$= \frac{1}{P^2} \sum_{i=1}^P \sum_{j=1}^P \mathbb{E}\{(\hat{\mathbf{e}}_i - \mathbf{e})^\top (\hat{\mathbf{e}}_j - \mathbf{e}) | \mathbf{y}\} \quad (\text{D.9})$$

$$= \frac{1}{P^2} \sum_{i=1}^P \mathbb{E}\{(\hat{\mathbf{e}}_i - \mathbf{e})^\top (\hat{\mathbf{e}}_i - \mathbf{e}) | \mathbf{y}\} + \frac{1}{P^2} \sum_{i=1}^P \sum_{j \neq i} \mathbb{E}\{(\hat{\mathbf{e}}_i - \mathbf{e})^\top (\hat{\mathbf{e}}_j - \mathbf{e}) | \mathbf{y}\} \quad (\text{D.10})$$

$$= \frac{1}{P^2} \sum_{i=1}^P [\mathbb{E}\{\|\hat{\mathbf{e}}_i\|^2 | \mathbf{y}\} - 2\mathbb{E}\{\hat{\mathbf{e}}_i^\top \mathbf{e} | \mathbf{y}\} + \mathbb{E}\{\|\mathbf{e}\|^2 | \mathbf{y}\}] \quad (\text{D.11})$$

$$+ \frac{1}{P^2} \sum_{i=1}^P \sum_{j \neq i} [\mathbb{E}\{\hat{\mathbf{e}}_i^\top \hat{\mathbf{e}}_j | \mathbf{y}\} - \mathbb{E}\{\hat{\mathbf{e}}_i^\top \mathbf{e} | \mathbf{y}\} - \mathbb{E}\{\mathbf{e}^\top \hat{\mathbf{e}}_j | \mathbf{y}\} + \mathbb{E}\{\|\mathbf{e}\|^2 | \mathbf{y}\}] \quad (\text{D.11})$$

$$= \frac{1}{P^2} \sum_{i=1}^P \mathbb{E}\{\|\hat{\mathbf{e}}_i\|^2 | \mathbf{y}\} + \frac{1}{P} \mathbb{E}\{\|\mathbf{e}\|^2 | \mathbf{y}\} + \frac{P(P-1)}{P^2} \mathbb{E}\{\|\mathbf{e}\|^2 | \mathbf{y}\}, \quad (\text{D.12})$$

where certain terms vanished because the i.i.d. and zero-mean properties of $\{\mathbf{e}, \hat{\mathbf{e}}_1, \dots, \hat{\mathbf{e}}_P\}$ imply

$$\mathbb{E}\{\hat{\mathbf{e}}_i^\top \hat{\mathbf{e}}_j | \mathbf{y}\} = \mathbb{E}\{\hat{\mathbf{e}}_i | \mathbf{y}\}^\top \mathbb{E}\{\hat{\mathbf{e}}_j | \mathbf{y}\} = 0 \quad (\text{D.13})$$

$$\mathbb{E}\{\hat{\mathbf{e}}_i^\top \mathbf{e} | \mathbf{y}\} = \mathbb{E}\{\hat{\mathbf{e}}_i | \mathbf{y}\}^\top \mathbb{E}\{\mathbf{e} | \mathbf{y}\} = 0 \quad (\text{D.14})$$

$$\mathbb{E}\{\mathbf{e}^\top \hat{\mathbf{e}}_j | \mathbf{y}\} = \mathbb{E}\{\mathbf{e} | \mathbf{y}\}^\top \mathbb{E}\{\hat{\mathbf{e}}_j | \mathbf{y}\} = 0. \quad (\text{D.15})$$

Finally, note that $\mathbb{E}\{\|\mathbf{e}\|^2 | \mathbf{y}\} = \mathcal{E}_{\text{mmse}}$ from (12) and (D.2). Furthermore, because $\{\mathbf{x}, \mathbf{x}_1, \dots, \mathbf{x}_P\}$ are independent samples of $p_{\mathbf{x}|\mathbf{y}}(\cdot | \mathbf{y})$ under the assumptions of Proposition 2, we have $\mathbb{E}\{\|\mathbf{e}\|^2 | \mathbf{y}\} = \mathbb{E}\{\|\hat{\mathbf{e}}_i\|^2 | \mathbf{y}\}$ and so (D.12) becomes

$$\mathcal{E}_P = \frac{1}{P^2} \sum_{i=1}^P \mathcal{E}_{\text{mmse}} + \frac{1}{P} \mathcal{E}_{\text{mmse}} + \frac{P(P-1)}{P^2} \mathcal{E}_{\text{mmse}} = \frac{P+1}{P} \mathcal{E}_{\text{mmse}}. \quad (\text{D.16})$$

This result holds for any $P \geq 1$, which implies the ratio

$$\frac{\mathcal{E}_P}{\mathcal{E}_1} = \frac{P+1}{2P}. \quad (\text{D.17})$$

E. CFID implementation details

Recall the CFID definition from (20):

$$\text{CFID} \triangleq \mathbb{E}_y \left\{ \|\boldsymbol{\mu}_{\hat{\mathbf{x}}|\mathbf{y}} - \boldsymbol{\mu}_{\hat{\mathbf{x}}|\mathbf{y}}\|_2^2 + \text{tr} \left[\boldsymbol{\Sigma}_{\hat{\mathbf{x}}\hat{\mathbf{x}}|\mathbf{y}} + \boldsymbol{\Sigma}_{\hat{\mathbf{x}}\hat{\mathbf{x}}|\mathbf{y}} - 2(\boldsymbol{\Sigma}_{\hat{\mathbf{x}}\hat{\mathbf{x}}|\mathbf{y}}^{1/2} \boldsymbol{\Sigma}_{\hat{\mathbf{x}}\hat{\mathbf{x}}|\mathbf{y}} \boldsymbol{\Sigma}_{\hat{\mathbf{x}}\hat{\mathbf{x}}|\mathbf{y}}^{1/2})^{1/2} \right] \right\}. \quad (\text{E.1})$$

The values used to compute (E.1) are [26]

$$\boldsymbol{\mu}_{\hat{\mathbf{x}}|\mathbf{y}} = \boldsymbol{\mu}_{\hat{\mathbf{x}}} + \boldsymbol{\Sigma}_{\hat{\mathbf{x}}\mathbf{y}} \boldsymbol{\Sigma}_{\mathbf{y}\mathbf{y}}^{-1} (\mathbf{y} - \boldsymbol{\mu}_{\mathbf{y}}) \quad (\text{E.2})$$

$$\boldsymbol{\Sigma}_{\hat{\mathbf{x}}\hat{\mathbf{x}}|\mathbf{y}} = \boldsymbol{\Sigma}_{\hat{\mathbf{x}}\hat{\mathbf{x}}} - \boldsymbol{\Sigma}_{\hat{\mathbf{x}}\mathbf{y}} \boldsymbol{\Sigma}_{\mathbf{y}\mathbf{y}}^{-1} \boldsymbol{\Sigma}_{\mathbf{y}\hat{\mathbf{x}}} \quad (\text{E.3})$$

$$\boldsymbol{\mu}_{\hat{\mathbf{x}}|\mathbf{y}} = \boldsymbol{\mu}_{\hat{\mathbf{x}}} + \boldsymbol{\Sigma}_{\hat{\mathbf{x}}\mathbf{y}} \boldsymbol{\Sigma}_{\mathbf{y}\mathbf{y}}^{-1} (\mathbf{y} - \boldsymbol{\mu}_{\mathbf{y}}) \quad (\text{E.4})$$

$$\boldsymbol{\Sigma}_{\hat{\mathbf{x}}\hat{\mathbf{x}}|\mathbf{y}} = \boldsymbol{\Sigma}_{\hat{\mathbf{x}}\hat{\mathbf{x}}} - \boldsymbol{\Sigma}_{\hat{\mathbf{x}}\mathbf{y}} \boldsymbol{\Sigma}_{\mathbf{y}\mathbf{y}}^{-1} \boldsymbol{\Sigma}_{\mathbf{y}\hat{\mathbf{x}}}, \quad (\text{E.5})$$

where $\boldsymbol{\Sigma}_{ij}$ denotes the cross-covariance for $i \neq j$ and the auto-covariance otherwise. Plugging the above values into (E.1), the CFID can be written as [26, Lemma 2]

$$\text{CFID} = \|\boldsymbol{\mu}_{\hat{\mathbf{x}}} - \boldsymbol{\mu}_{\hat{\mathbf{x}}}\|_2^2 + \text{tr} \left[(\boldsymbol{\Sigma}_{\hat{\mathbf{x}}\mathbf{y}} - \boldsymbol{\Sigma}_{\hat{\mathbf{x}}\mathbf{y}}) \boldsymbol{\Sigma}_{\mathbf{y}\mathbf{y}}^{-1} (\boldsymbol{\Sigma}_{\mathbf{y}\hat{\mathbf{x}}} - \boldsymbol{\Sigma}_{\mathbf{y}\hat{\mathbf{x}}}) \right] + \text{tr} \left[\boldsymbol{\Sigma}_{\hat{\mathbf{x}}\hat{\mathbf{x}}|\mathbf{y}} + \boldsymbol{\Sigma}_{\hat{\mathbf{x}}\hat{\mathbf{x}}|\mathbf{y}} - 2(\boldsymbol{\Sigma}_{\hat{\mathbf{x}}\hat{\mathbf{x}}|\mathbf{y}}^{1/2} \boldsymbol{\Sigma}_{\hat{\mathbf{x}}\hat{\mathbf{x}}|\mathbf{y}} \boldsymbol{\Sigma}_{\hat{\mathbf{x}}\hat{\mathbf{x}}|\mathbf{y}}^{1/2})^{1/2} \right], \quad (\text{E.6})$$

where the inverse Σ_{yy}^{-1} is typically implemented using a pseudo-inverse Σ_{yy}^+ .

In practice, when computing CFID, we have a set of test data, $\{\mathbf{x}_t, \mathbf{y}_t\}_{t=1}^n$ and, for each \mathbf{y}_t , we have a set of generated test samples $\{\widehat{\mathbf{x}}_{ti}\}_{i=1}^P$. We repeat \mathbf{x}_t and \mathbf{y}_t P times, which yields a new set of P tuples, $\{\mathbf{x}_{ti}, \mathbf{y}_{ti}, \widehat{\mathbf{x}}_{ti}\}_{i=1}^P$ for $t = 1 \dots n$. We embed all \mathbf{x}_{ti} , \mathbf{y}_{ti} , and $\widehat{\mathbf{x}}_{ti}$ using a feature-generating network, yielding embedding matrices \mathbf{X} , \mathbf{Y} , and $\widehat{\mathbf{X}}$ of dimension $Pn \times d$, respectively. We used the VGG-16 network [24] for our MRI experiments, since [13] found that it gave results that correlated much better with radiologists' perceptions, while we used the standard Inception-v3 network [30] for our inpainting experiments. The embeddings are then used to compute the sample mean values

$$\begin{aligned}\boldsymbol{\mu}_{\mathbf{x}} &= \frac{1}{Pn} \sum_{i=1}^{Pn} \mathbf{X}_i \\ \boldsymbol{\mu}_{\mathbf{y}} &= \frac{1}{Pn} \sum_{i=1}^{Pn} \mathbf{Y}_i \\ \boldsymbol{\mu}_{\widehat{\mathbf{x}}} &= \frac{1}{Pn} \sum_{i=1}^{Pn} \widehat{\mathbf{X}}_i.\end{aligned}\tag{E.7}$$

We use the values from (E.7) to subtract the mean from each row of \mathbf{X} , \mathbf{Y} , and $\widehat{\mathbf{X}}$, yielding a new set of zero-mean embedding matrices $\underline{\mathbf{X}}$, $\underline{\mathbf{Y}}$, and $\underline{\widehat{\mathbf{X}}}$, respectively. Then, $\underline{\mathbf{X}}$, $\underline{\mathbf{Y}}$, and $\underline{\widehat{\mathbf{X}}}$ are used to compute the sample auto-covariance matrices

$$\begin{aligned}\Sigma_{\mathbf{xx}} &= \frac{1}{Pn} \underline{\mathbf{X}}^T \underline{\mathbf{X}} \\ \Sigma_{\mathbf{yy}} &= \frac{1}{Pn} \underline{\mathbf{Y}}^T \underline{\mathbf{Y}} \\ \Sigma_{\widehat{\mathbf{xx}}} &= \frac{1}{Pn} \underline{\widehat{\mathbf{X}}}^T \underline{\widehat{\mathbf{X}}}\end{aligned}\tag{E.8}$$

and the sample cross-covariance matrices

$$\begin{aligned}\Sigma_{\mathbf{xy}} &= \frac{1}{Pn} \underline{\mathbf{X}}^T \underline{\mathbf{Y}} & \Sigma_{\mathbf{yx}} &= \frac{1}{Pn} \underline{\mathbf{Y}}^T \underline{\mathbf{X}} \\ \Sigma_{\widehat{\mathbf{xy}}} &= \frac{1}{Pn} \underline{\widehat{\mathbf{X}}}^T \underline{\mathbf{Y}} & \Sigma_{\widehat{\mathbf{yx}}} &= \frac{1}{Pn} \underline{\mathbf{Y}}^T \underline{\widehat{\mathbf{X}}}.\end{aligned}\tag{E.9}$$

We plug the sample statistics from (E.8) and (E.9) into (E.3) and (E.5) to compute the conditional covariance matrices, which are then used in conjunction with the values from (E.7), (E.8), and (E.9) to compute the CFID as written in (E.6). In [26], the authors use $P = 1$ in all of their experiments. To be consistent with how we evaluated the other metrics, we use $P = 32$ unless otherwise noted.

F. MR imaging details

We now present some details about the MR imaging linear inverse problem. Suppose that the goal is to recover the N -pixel MR image $\mathbf{i} \in \mathbb{C}^N$ from the multicoil measurements $\{\mathbf{k}_c\}_{c=1}^C$, where [20]

$$\mathbf{k}_c = \mathbf{MFS}_c \mathbf{i} + \mathbf{n}_c.\tag{F.1}$$

In (F.1), C refers to the number of coils, $\mathbf{k}_c \in \mathbb{C}^M$ are the measurements from the c th coil, $\mathbf{M} \in \mathbb{R}^{M \times N}$ is a sub-sampling operator containing rows from \mathbf{I}_N —the $N \times N$ identity matrix, $\mathbf{F} \in \mathbb{C}^{N \times N}$ is the unitary 2D discrete Fourier transform, $\mathbf{S}_c \in \mathbb{C}^{N \times N}$ is a diagonal matrix containing the sensitivity map of the c th coil, and $\mathbf{n}_c \in \mathbb{C}^M$ is noise. From (F.1), it can be seen that the MR measurements are collected in the spatial Fourier domain, otherwise known as the “k-space.” We assume that the sensitivity maps $\{\mathbf{S}_c\}$ are estimated from $\{\mathbf{k}_c\}$ using ESPiRiT [32], which yields maps with the property $\sum_{c=1}^C \mathbf{S}_c^H \mathbf{S}_c = \mathbf{I}_N$. The ratio $R \triangleq \frac{N}{M}$ is known as the acceleration rate.

There are different ways that one could apply the generative posterior sampling framework to multicoil MR image recovery. One is to configure the generator to produce posterior samples $\widehat{\mathbf{i}}$ of the complex image \mathbf{i} . Another is to configure the generator to produce posterior samples $\widehat{\mathbf{x}}$ of the stack $\mathbf{x} \triangleq [\mathbf{x}_1^T, \dots, \mathbf{x}_C^T]^T$ of “coil images” $\mathbf{x}_c \triangleq \mathbf{S}_c \mathbf{i}$ and later coil-combining them to yield a complex image estimate $\widehat{\mathbf{i}} \triangleq [\mathbf{S}_1^H, \dots, \mathbf{S}_C^H] \widehat{\mathbf{x}}$. We take the latter approach. Furthermore, rather than feeding our generator with k-space measurements \mathbf{k}_c , we choose to feed it with aliased coil images $\mathbf{y}_c \triangleq \mathbf{F}^H \mathbf{M}^T \mathbf{k}_c$. Writing (F.1) in terms of the coil images, we obtain

$$\mathbf{y}_c = \mathbf{F}^H \mathbf{M}^T \mathbf{M} \mathbf{F} \mathbf{x}_c + \mathbf{w}_c,\tag{F.2}$$

where $\mathbf{w}_c \triangleq \mathbf{F}^H \mathbf{M}^T \mathbf{n}_c$. Then we can stack $\{\mathbf{y}_c\}$ and $\{\mathbf{w}_c\}$ column-wise into vectors \mathbf{y} and \mathbf{w} , and set $\mathbf{A} = \mathbf{I}_C \otimes \mathbf{F}^H \mathbf{M}^T \mathbf{M} \mathbf{F} \in \mathbb{C}^{NC \times NC}$, to obtain the formulation in (1).

To train our generator, we assume to have access to paired training examples $\{(\mathbf{x}_t, \mathbf{y}_t)\}$, where \mathbf{x}_t is a stack of coil images and \mathbf{y}_t is the corresponding stack of k-space coil measurements. The fastMRI multicoil dataset [36] provides $\{(\mathbf{x}_t, \mathbf{k}_t)\}$, from which we can easily obtain $\{(\mathbf{x}_t, \mathbf{y}_t)\}$.

To implement the data-consistency method in (33), we note that $\mathbf{A} = \mathbf{I}_C \otimes \mathbf{F}^H \mathbf{M}^T \mathbf{M} \mathbf{F}$ is an orthogonal projection matrix, and so $\mathbf{I} - \mathbf{A}^+ \mathbf{A} = \mathbf{I} - \mathbf{A} = \mathbf{I} \otimes \mathbf{F}^H (\mathbf{I} - \mathbf{M}^T \mathbf{M}) \mathbf{F}$.

G. Network implementation details

G.1. MRI

Generator architecture. For our MRI experiments, we take inspiration from the U-Net architecture [22], using it as the basis for our generator. The primary input, \mathbf{y} is concatenated with the code vector \mathbf{z} and fed through the U-Net. The network consists of 4 pooling layers with 128 initial channels. However, instead of pooling we opt to use convolutions with filters of size 3×3 , “same” padding, and a stride of 2 when downsampling. Conversely, we upsample using transpose convolutions, again with filters of size 3×3 , “same” padding, and a stride of 2. All other convolutions utilize filters of size 3×3 , “same” padding, and a stride of 1.

Within each encoder and decoder layer we include a residual block, the architecture of which can be found in [1]. We use instance-norm for all normalization layers and parametric ReLUs as our activation functions, in which the network learns the optimal “negative slope.” Finally, we include 5 residual blocks at the base of the U-Net, in between the encoder and decoder. This is done in an effort to artificially increase the depth of the network and is inspired by [5]. Our generator has 86 734 334 trainable parameters.

Discriminator architecture. Our discriminator is a standard CNN with 5 layers. In the first 3 layers, we use convolutions with filter of size 4×4 , “same” padding, and a stride of 2 to reduce the image resolution. The remaining two convolutional layers use the same parameters, with the stride modified to be 1. We use batch-norm as our normalization layer and leaky ReLUs with a “negative-slope” of 0.2 as our activation functions.

The final convolutional layer does not have a normalization layer or activation function, and outputs a 1 channel “prediction map.” This prediction map gives a Wasserstein score for a patch of the image. We achieve this patch-based discrimination by utilizing the receptive field of the network. Consequently, by increasing or decreasing the number of strided convolutions we use, we can modify the size of the patches we are discriminating. Patch-based discrimination has been known to improve the high-frequency information in reconstructions [9]. Our discriminator has 693 057 trainable parameters.

cGANs. For all 3 cGANs, we use the architectures described above, as well as the same, or a similar, training/testing procedure. We adapt the model’s regularization and β_{adv} to match the authors’ original implementation. In particular, when training Ohayon et al.’s cGAN we set $\beta_{\text{adv}} = 1e-3$ and use $\mathcal{L}_{2,P}$ regularization while training the generator. When training Adler et al.’s cGAN, we set $\beta_{\text{adv}} = 1$ and do not apply any regularization to the generator. Instead we modify the number of input channels to the discriminator and slightly modify the training logic to be consistent with the loss proposed in (7).

Langevin. For Jalal et al.’s approach [11], we do not modify the original implementation from [10] other than replacing the default sampling pattern with the GRO undersampling mask. We generated 32 samples for 72 different test images using a batch-size of 4, which took roughly 6 days. These samples were generated on a server with 4 NVIDIA V100 GPUs, each with 32 GB of memory. We used 4 samples per batch (and recorded the time to generate 4 samples in Table 1) because the code from [10] is written to generate one sample per GPU.

G.2. Inpainting

CoModGAN. We used the PyTorch implementation of CoModGAN from [37] and trained the model to inpaint a 64×64 centered square (not accept an arbitrary mask). The total training time on a server with 4 NVIDIA A100 GPUs, each with 82 GB of memory, was roughly 1.5 days.

Langevin. For Song et al.’s Langevin approach [27], we use the official PyTorch implementation from [28]. We trained the NCSNv2 model using the celebA configuration with our 128×128 celebA-HQ data using a batch-size of 32. We generated 32 samples for all 1000 images in our test set, using a batch-size of 40 and generating 32 samples for each batch element concurrently. The total running time on a server with 4 NVIDIA A100 GPUs, each with 82 GB of memory, was roughly 4 days.

G.3. Additional CFID results

We can write the CFID from (20) as a sum of two terms: a term that quantifies the conditional-mean error and a term that quantifies the conditional-covariance error:

$$\text{CFID} = \text{CFID}_{\text{mean}} + \text{CFID}_{\text{cov}} \tag{G.1}$$

$$\text{CFID}_{\text{mean}} \triangleq \mathbb{E}_{\mathbf{y}} \{ \|\boldsymbol{\mu}_{\mathbf{x}|\mathbf{y}} - \boldsymbol{\mu}_{\widehat{\mathbf{x}}|\mathbf{y}}\|_2^2 \} \tag{G.2}$$

$$\text{CFID}_{\text{cov}} \triangleq \text{tr} \left[\boldsymbol{\Sigma}_{\mathbf{xx}|\mathbf{y}} + \boldsymbol{\Sigma}_{\widehat{\mathbf{x}}|\mathbf{y}} - 2(\boldsymbol{\Sigma}_{\mathbf{xx}|\mathbf{y}}^{1/2} \boldsymbol{\Sigma}_{\widehat{\mathbf{x}}|\mathbf{y}} \boldsymbol{\Sigma}_{\mathbf{xx}|\mathbf{y}}^{1/2})^{1/2} \right]. \tag{G.3}$$

Table G.1. The mean and covariance components of CFID for the cGANs in the MRI and inpainting experiments. For the MRI experiment, CFID¹ used 72 test samples and $P = 32$, CFID² used 2376 test samples and $P = 8$, and CFID³ used all 14 576 samples and $P = 1$. For the inpainting experiment, CFID¹ used 1000 test images and $P = 32$, CFID² used 3000 test and validation images and $P = 8$, and CFID³ used all 30 000 images and $P = 1$.

Experiment	Model	CFID ¹ _{mean} ↓	CFID ¹ _{cov} ↓	CFID ² _{mean} ↓	CFID ² _{cov} ↓	CFID ³ _{mean} ↓	CFID ³ _{cov} ↓
MRI	Adler et al. [1]	1.54	2.22	2.27	1.00	2.29	0.66
	Ohayon et al. [17]	2.77	3.43	2.79	1.48	2.71	1.10
	Ours	0.85	2.09	0.86	0.68	0.86	0.43
Inpainting	CoModGAN [41]	0.30	39.45	0.32	23.94	0.31	4.63
	Ours	0.59	39.07	0.44	22.10	0.41	4.30

In Table G.1, we report CFID_{mean} and CFID_{cov} for the MRI and inpainting experiments. As before, we computed CFID on several data subsets for each experiment, motivated by the fact that the CFID bias decreases as the number of data samples increases [26]. For the MRI experiment, Table G.1 shows that our proposed method outperformed the other methods under test in both the mean and covariance components of CFID. For the inpainting experiment, Table G.1 shows that our proposed method outperformed CoModGAN in the covariance component of CFID but not the mean component of CFID. In the inpainting experiment, we believe that the covariance component is more important than the mean component, because the goal of large-scale inpainting is not to recover the original image but rather to hallucinate diverse faces that are consistent with the unmasked pixels.

H. Additional reconstruction plots

H.1. MRI

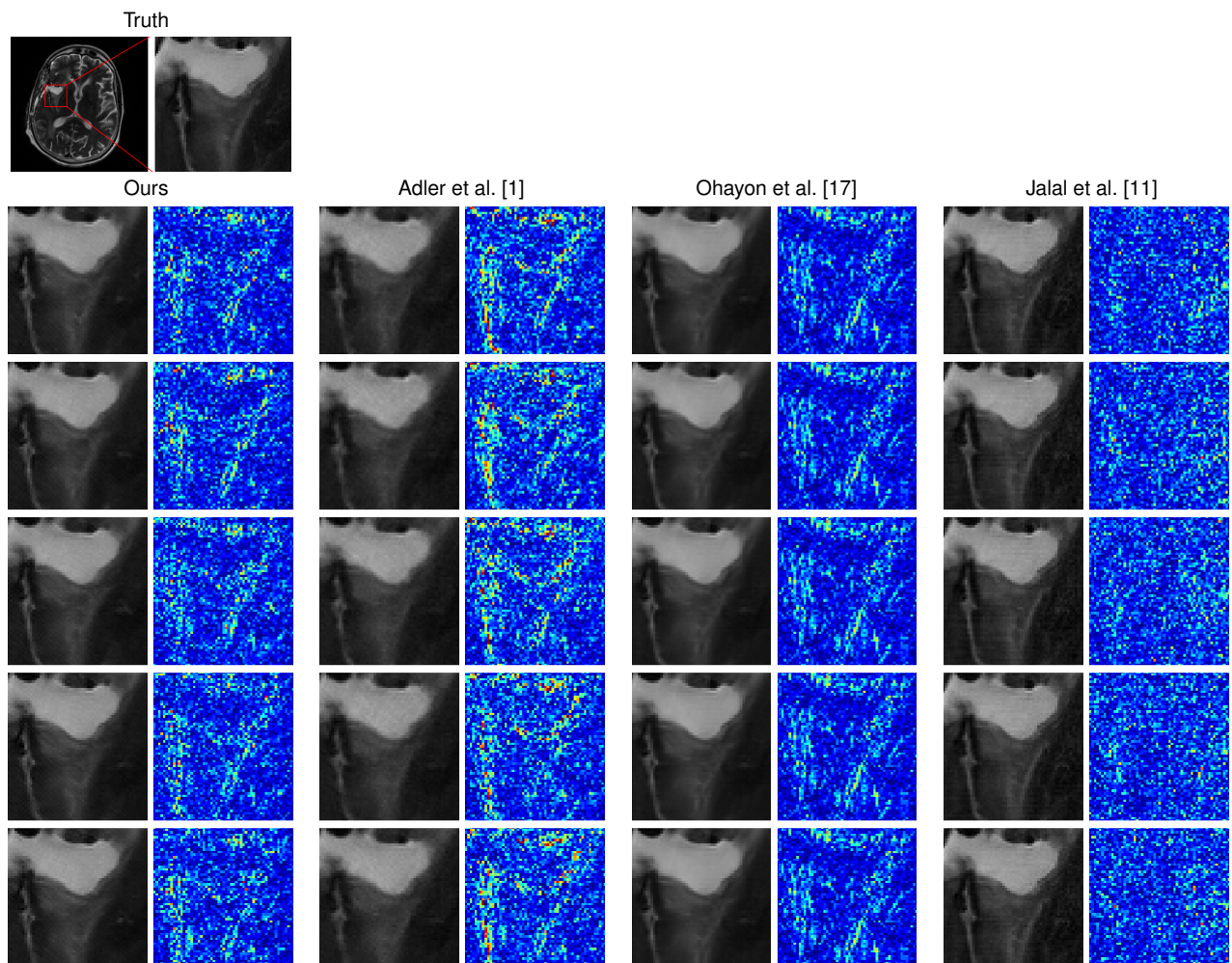


Figure H.1. Example posterior samples of a zoomed region. The first column for each method contains five samples, and the second contains the corresponding error map. The purpose of the error map is to better identify variation across samples.

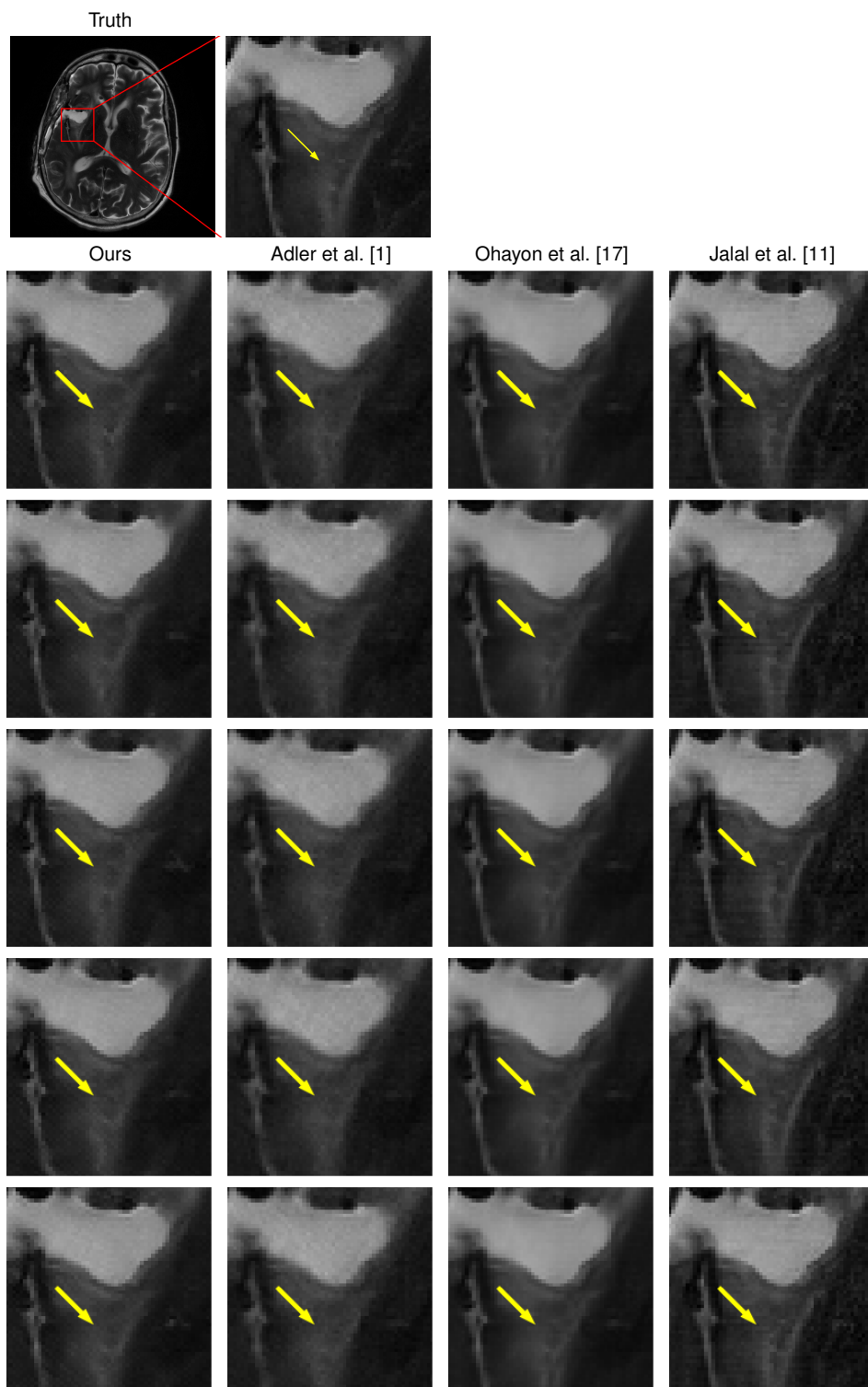


Figure H.2. Example posterior samples of a zoomed region. Visible variation in an anatomical feature is highlighted by yellow arrows.

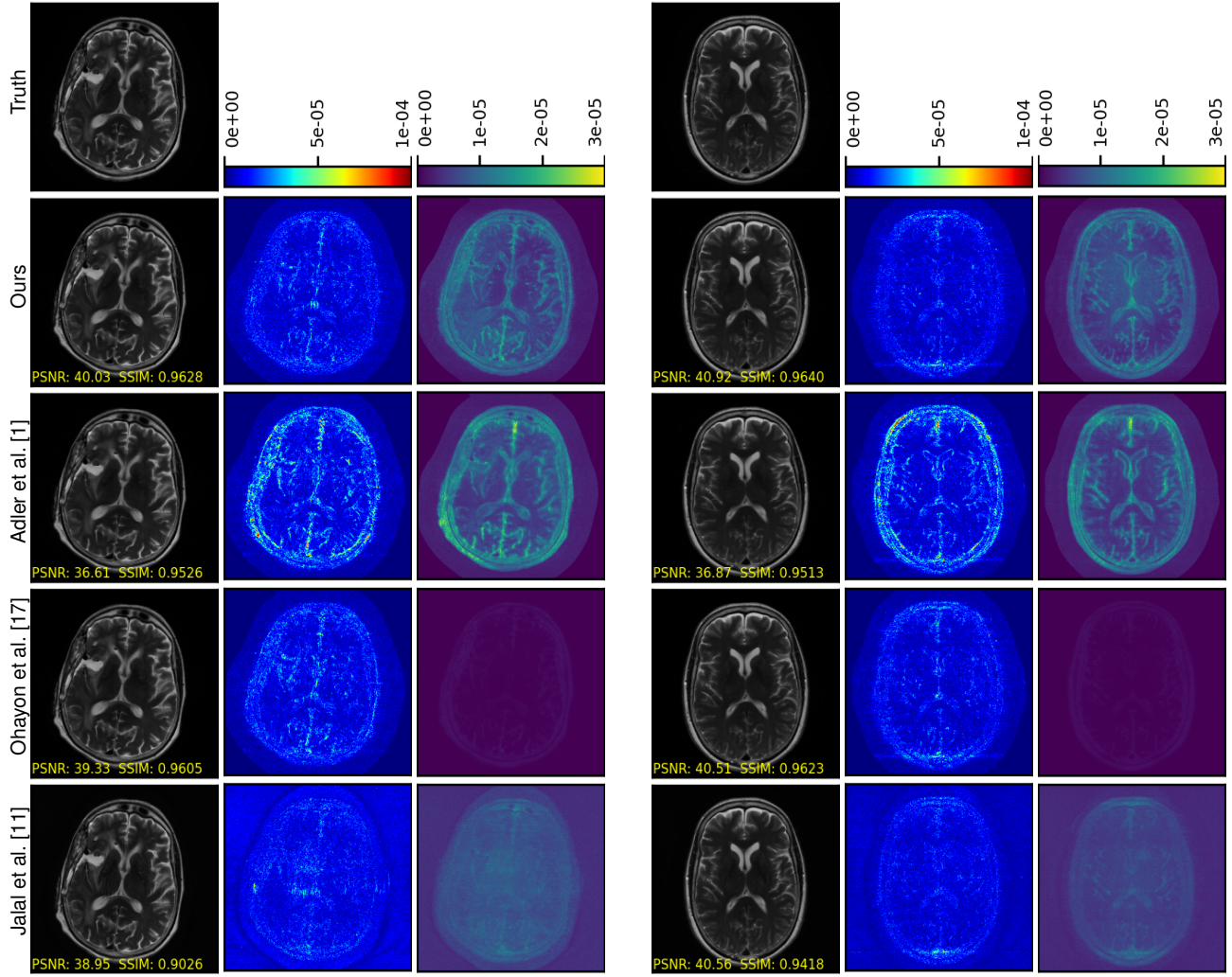


Figure H.3. MRI reconstruction of two test images. Column one: reconstruction $\hat{\mathbf{x}}_{(P)}$, two: pixel-wise absolute error $|\hat{\mathbf{x}}_{(P)} - \mathbf{x}|$, three: pixel-wise standard-deviation $(\frac{1}{P} \sum_{i=1}^P (\hat{\mathbf{x}}_i - \hat{\mathbf{x}}_{(P)})^2)^{1/2}$.

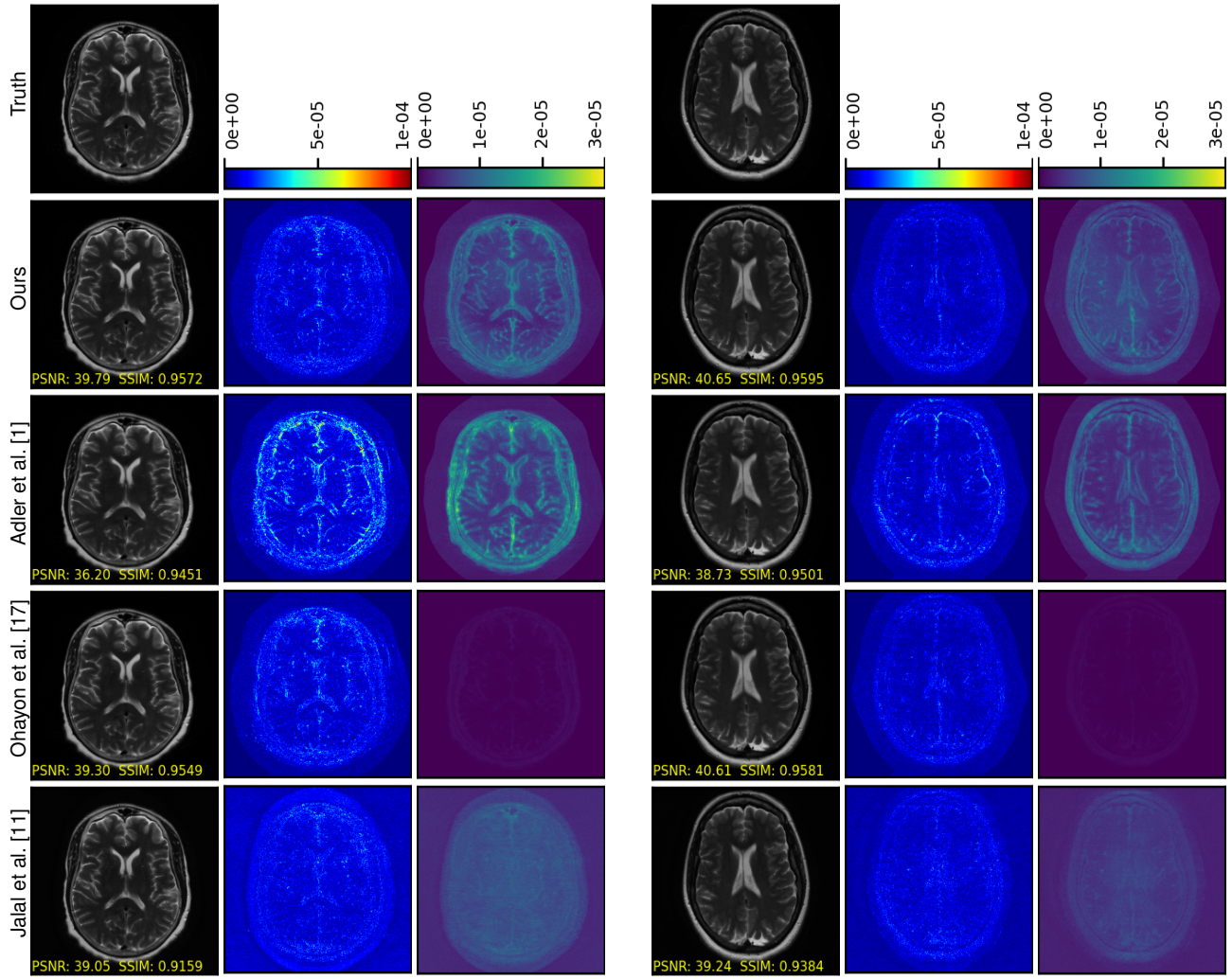


Figure H.4. MRI reconstruction of two test images. Column one: reconstruction $\hat{\mathbf{x}}_{(P)}$, two: pixel-wise absolute error $|\hat{\mathbf{x}}_{(P)} - \mathbf{x}|$, three: pixel-wise standard-deviation $(\frac{1}{P} \sum_{i=1}^P (\hat{\mathbf{x}}_i - \hat{\mathbf{x}}_{(P)})^2)^{1/2}$.

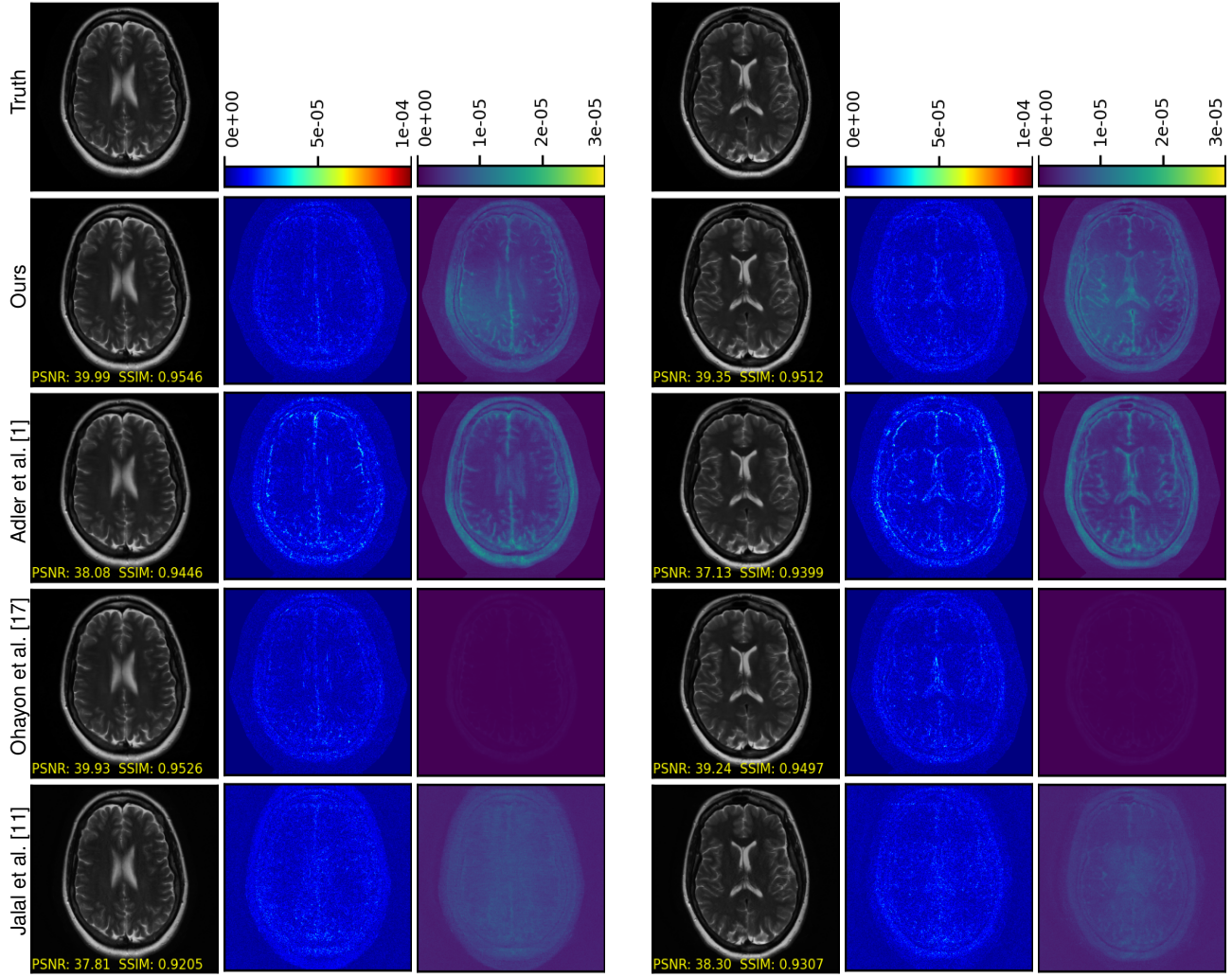


Figure H.5. MRI reconstruction of two test images. Column one: reconstruction $\hat{\mathbf{x}}_{(P)}$, two: pixel-wise absolute error $|\hat{\mathbf{x}}_{(P)} - \mathbf{x}|$, three: pixel-wise standard-deviation $(\frac{1}{P} \sum_{i=1}^P (\hat{\mathbf{x}}_i - \hat{\mathbf{x}}_{(P)})^2)^{1/2}$.

H.2. Inpainting

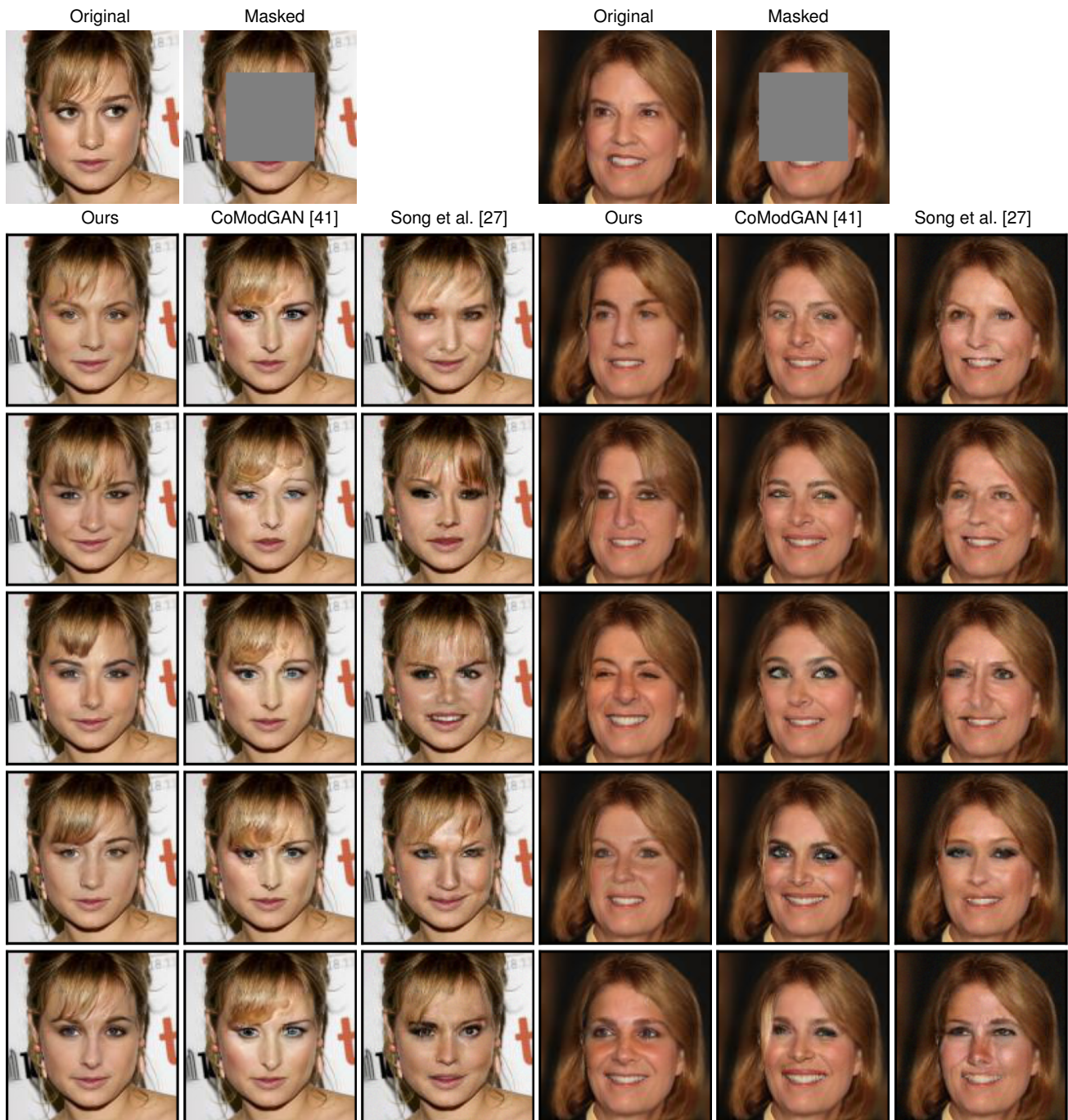


Figure H.6. Two examples of inpainting a 64×64 centered square on a 128×128 resolution celebA-HQ test image.

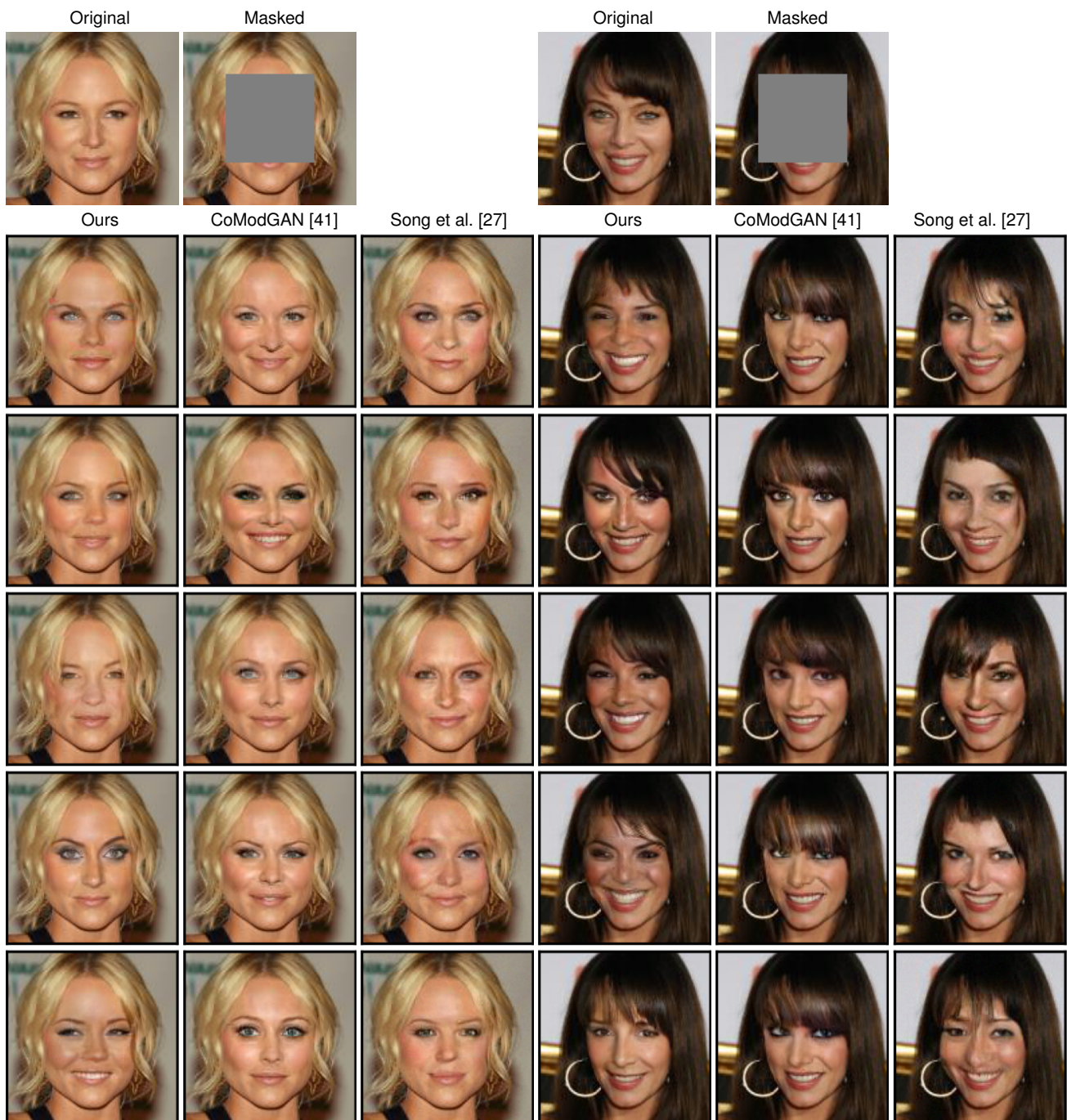


Figure H.7. Two examples of inpainting a 64×64 centered square on an 128×128 resolution celebA-HQ test image.

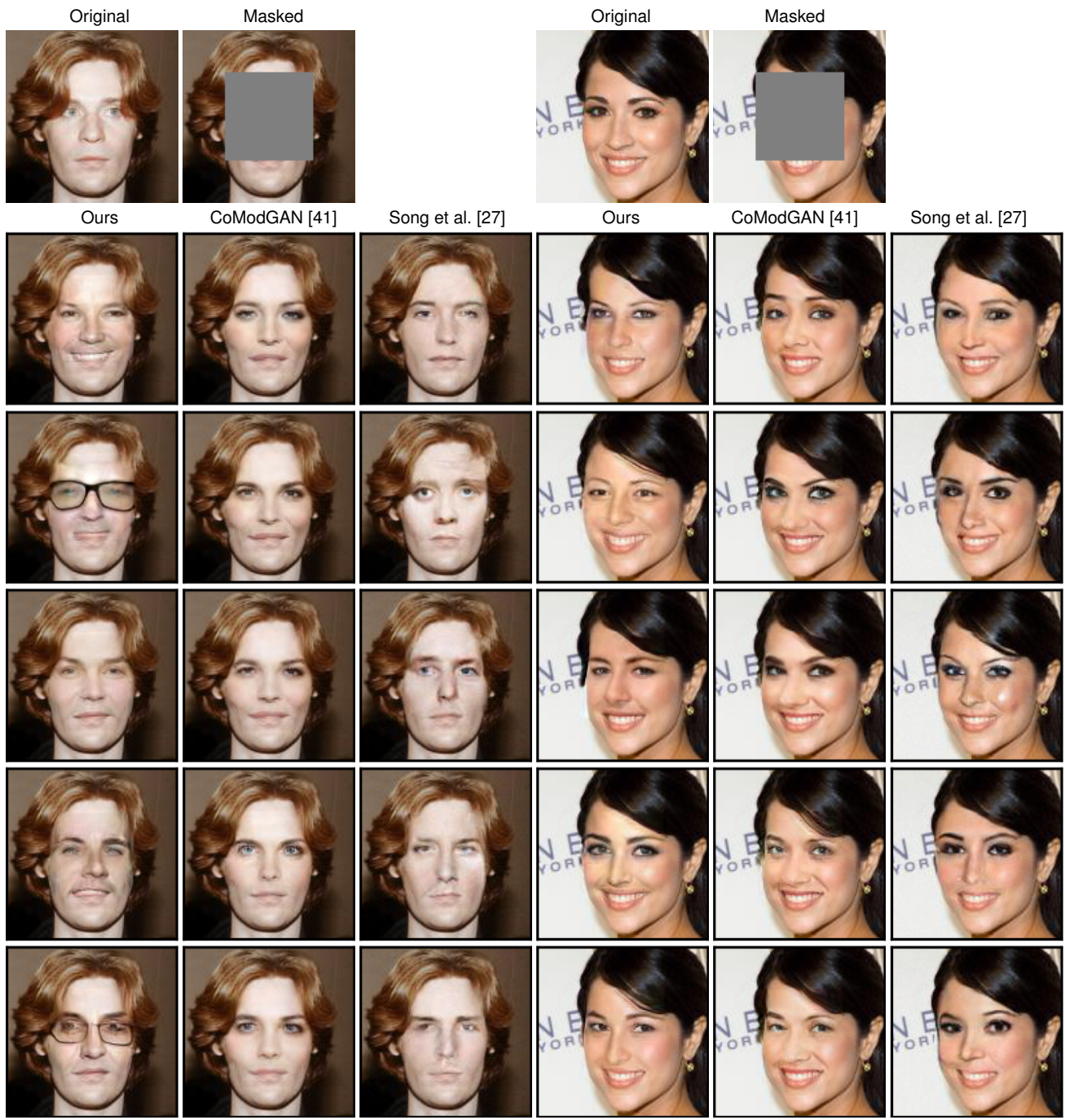


Figure H.8. Two examples of inpainting a 64×64 centered square on an 128×128 resolution celebA-HQ test image.

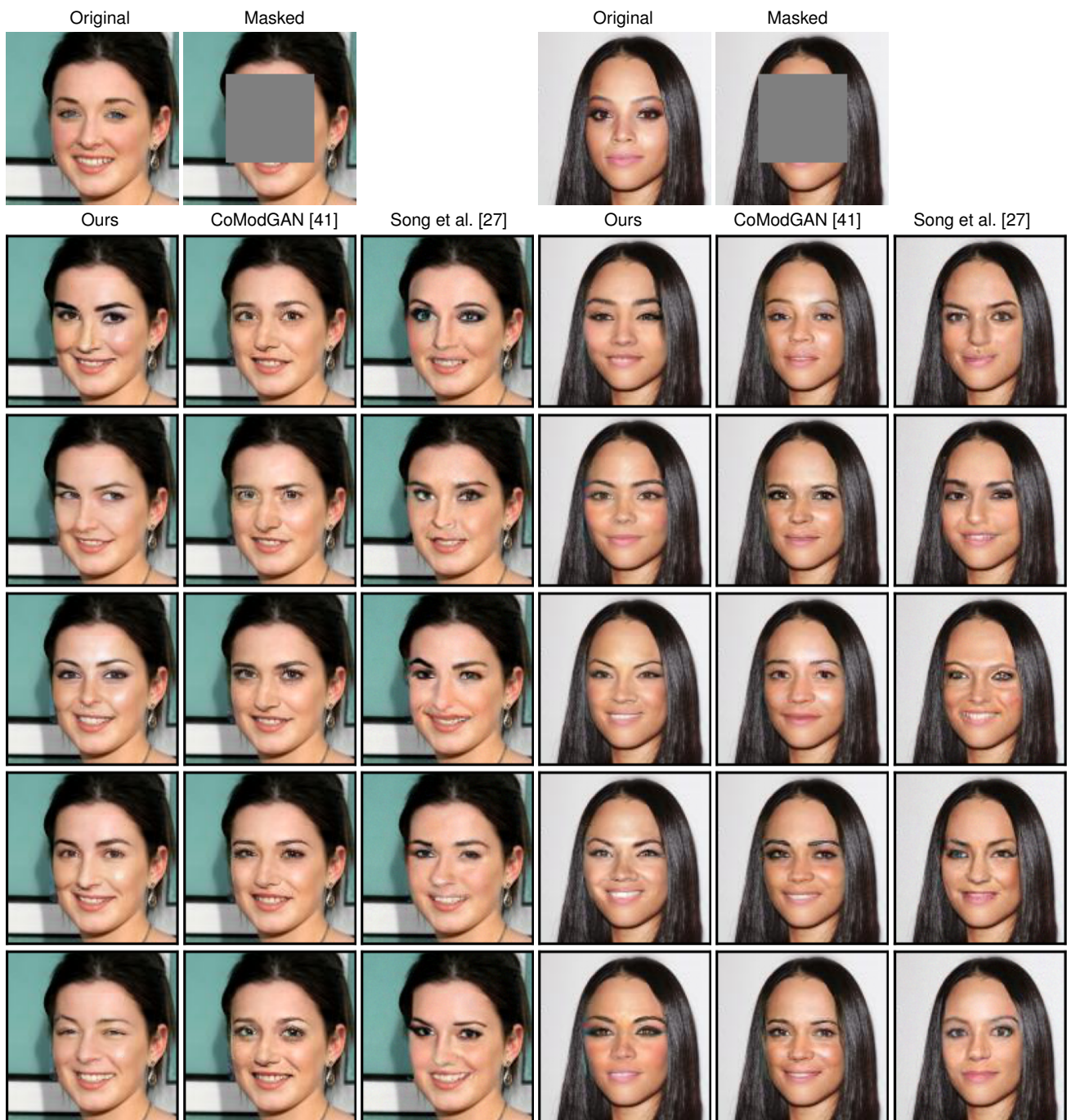


Figure H.9. Two examples of inpainting a 64×64 centered square on an 128×128 resolution celebA-HQ test image.